applied optics

Evaluation and characterization of imaging polarimetry through metasurface polarization gratings

LISA W. LI,[1] NOAH A. RUBIN,[1,*] MICHAEL JUHL,[1,2] JOON SUH PARK,[1,3] AND FEDERICO CAPASSO[1]

[1]Harvard John A. Paulson School of Engineering and Applied Sciences, Harvard University, Cambridge, Massachusetts 02138, USA
[2]NIL Technology, 2800 Kongens Lyngby, Denmark
[3]Nanophotonics Research Centre, Korea Institute of Science and Technology, Seoul, Republic of Korea
*noahrubin@seas.harvard.edu

Received 21 November 2022; revised 18 January 2023; accepted 19 January 2023; posted 24 January 2023; published 22 February 2023

Metasurfaces are a new class of diffractive optical elements with subwavelength elements whose behavior can be lithographically tailored. By leveraging form birefringence, metasurfaces can serve as multifunctional freespace polarization optics. Metasurface gratings are novel, to the best of our knowledge, polarimetric components that integrate multiple polarization analyzers into a single optical element enabling the realization of compact imaging polarimeters. The promise of metasurfaces as a new polarization building block is contingent on the calibration of metagrating-based optical systems. A prototype metasurface full Stokes imaging polarimeter is compared to a benchtop reference instrument using an established linear Stokes test for 670, 532, and 460 nm gratings. We propose a complementary full Stokes accuracy test and demonstrate it using the 532 nm grating. This work presents methods and practical considerations involved in producing accurate polarization data from a metasurface-based Stokes imaging polarimeter and informs their use in polarimetric systems more generally.

https://doi.org/10.1364/AO.480487

1. INTRODUCTION

Polarization is a fundamental property of electromagnetic radiation that is key to the study of optics and science more generally. Consequently, instruments designed to measure light's polarization state—known as polarimeters—are important tools for a wide spate of technological and scientific problems [1,2] in areas as diverse as remote sensing of clouds and aerosols [3,4], characterization of solar magnetic fields [5], liquid crystal panel quality control [6], 3D image reconstruction [7], and as a possible future means of biometric authentication in consumer electronics [8] (to name only a few).

Metasurfaces are a new class of freespace optics that manipulate light using subwavelength-spaced, single layer diffractive optical elements [9,10]. The individual subwavelength structures comprising a metasurface can be designed with form or shape birefringence, that is, birefringence resulting from the anisotropic shape of otherwise isotropic materials rather than an effect of crystalline structure. When suitably designed, metasurfaces can realize a variety of multi-functional polarization optics [11]. More specifically, polarization metasurface gratings—also referred to as polarization metagratings—can direct polarized light into diffraction orders that act as polarization analyzers for a selected set of polarization states [12,13]. In this way, a metasurface grating can be used as a single element polarimetric component that analyzes incoming polarized light along several polarization states in parallel, yielding sufficient information to determine its polarization state (in the form of the full Stokes vector). As polarimetric components, metasurfaces offer several design advantages: reduced system complexity/fewer optical elements, the ability to realize analysis along an arbitrarily selected set of polarization states, and the potential for increased efficiency over absorptive polarization elements.

While metasurfaces have been extensively demonstrated as polarimetric components and even in working polarization cameras for imagery of real-world scenes, relatively little consideration has been given to the accuracy (beyond a qualitative sense of correspondence) with which polarization can be measured using a metasurface polarimeter. In some ways, this is a more general concern. Despite polarization's fundamental role in the description of light, the effort dedicated to polarimetry pales in comparison to other types of optical metrology, especially spectroscopy. Fledgling standardization efforts for this topic pertain to instrument- and application-specific needs, such as in fiber-optic telecommunications [14], machine vision [15], and polarized microscopy [16]. Consequently, there are at present no universally accepted standards (NIST, industrial, or otherwise) pertaining to polarimetric accuracy or precision.

Quantitative polarimetry is complicated by the vectorial, higher-dimensional nature of polarization itself. For the myriad areas where polarization finds application, in each place, there are vastly different requirements on polarimetric measurement. It is challenging to define the performance of a given polarimeter with any one readily intuited specification that corresponds to a practically meaningful interpretation. The standards by which a polarimeter's performance should be evaluated are then contingent upon what conclusions are desired from its data.

Across all application domains in which polarimetry is used, scientific remote sensing applications tend to harbor the most quantitative and specific requirements and come closest to this ideal. One area in particular that has influenced the present work is polarimetric remote sensing of clouds and aerosols. In atmospheric science, space- and aircraft-based remotely sensed imagery of small particles is obtained at multiple viewing angles and wavelengths. These images are used in conjunction with forward radiative transfer modeling to constrain useful properties of small particles in the atmosphere such as aerosol optical depth, refractive index, and type. These and other crucial variables enter into larger radiative forcing models for the prediction of global climate change. Polarization can better constrain these retrievals, and polarimetry is now an established technique in atmospheric remote sensing with several instruments launched into orbit since the 1990s [4], such as Polarization and Directionality of the Earth's Reflectances (POLDER) (I, II, and III) [17,18], Hyper-Angular Rainbow Polarimeter (HARP) CubeSat [19–21], and the upcoming Multi-Angle Imager for Aerosols (MAIA) [22–24], Multi-viewing, Multi-channel, Multi-polarisation Imager (3MI) [25], and Spectro-polarimeter for Planetary Exploration (SPEX) [26,27] missions, alongside countless airborne instruments—all of them sensing just the linear part of light's polarization state. Addressing how exactly errors in the measured polarization state (both random and systematic in nature) influence these retrieved parameters and how much error tolerance is allowed to achieve the data's end goals involves performing sensitivity analysis on what is a complex and highly context-dependent inverse problem. A few works, however, investigated this explicitly [28,29], leading to an often-cited figure that the degree of linear polarization (DOLP) determined by a polarimeter should be accurate to within 0.5% to serve the needs of multi-angular atmospheric polarimetry. This figure, while unquestionably an incomplete metric by itself, has become the *de facto* standard in this area, as enshrined in NASA's Aerosols & Clouds-Convection-Precipitation Study (A&CCP) and its Science & Applications Traceability Matrix in response to the most recent Decadal Survey in 2017, which broadly governs instrument objectives in this area. Alongside this simply stated metric, the atmospheric polarimetry community has settled on an accompanying test experiment, involving the preparation of partially linearly polarized light with a tilted glass plate, referenced to a rotating-polarizer polarimeter [23,27,30]—a semi-standardized protocol used in this work.

In characterizing the full polarization state of light, that is, all four Stokes components, no similarly clear-cut, widely accepted metric exists. Light's full polarization state (including circular polarization) has seen use in a number of remote sensing applications, especially in astronomy. For instance, it has been observed that planetary atmospheres natively exhibit a degree of circular polarization (DOCP) (due to multiple scattering) at the level of 10^{-7} [31]. In the field of solar polarimetry, full Stokes measurements are widely used to study the sun's magnetic fields [5]. Quantitative, full Stokes error analyses tend to involve rigorous component-by-component polarimetric calibration in a way that can be expressed only in full matrix form (see, e.g., [32]).

If metasurfaces are to serve a role in future polarimetric instruments, then efforts must be undertaken to demonstrate that a well-calibrated metasurface-based polarimeter can perform polarimetry with some baseline of accuracy. Therefore, in the subsections that follow, we perform a quantitative evaluation of a metasurface polarimeter with respect to reference measurements. We present two accuracy studies: the first, concerning linear-only polarimetry, uses the tilted plate test described above; the second, characterizing the accuracy with which circular polarization may be determined, makes use of light produced by a rotating retarder in a method we describe below. Together, these tests reveal the accuracy with which a metasurface-based polarimeter can determine light's polarization state. This work also illuminates a number of important practical considerations surrounding polarimetric calibration of metasurface-based instruments and suitable reference measurements.

We begin in Section 2 by defining some polarization conventions used throughout this work. In Section 3, we describe the metasurface-based imaging polarimeters under study here, including certain constraints that govern its design. In Section 4, we describe three metasurface diffraction grating samples for operation in three visible wavelength bands that are studied in this work. In Section 5, we describe two calibration schemes for metagrating-based cameras for linear-only and full Stokes determination. In Section 6, we describe two studies by which the accuracy of our considered metasurface-based imaging polarimeter can be ascertained (again, both linear-only and full Stokes). Finally, we conclude in Section 7, and provide extensive explanations of more detailed aspects of our measurements in Appendices A–F and Supplement 1.

2. POLARIZATION CONVENTIONS

This section briefly introduces the polarimetric quantities discussed in this work and establishes notation conventions. This work follows the notation convention from [33].

Mueller calculus is a method of describing fully polarized, partially polarized, and depolarized light and associated light–matter interactions using Mueller matrix and Stokes vectors. The 4×4 Mueller matrix $\mathbf{M}(\lambda, \hat{\mathbf{k}}_i, \hat{\mathbf{k}}_o, \hat{\eta})$ describes the polarimetric interaction between a subject and the illuminating light and is dependent on wavelength λ, incident propagation vector $\hat{\mathbf{k}}_i$, outgoing propagation vector $\hat{\mathbf{k}}_o$, and surface normal $\hat{\eta}$. Matrix multiplication with a Stokes vector is used to describe a light–matter interaction in scattering, transmitting, or reflecting geometries.

The Stokes vector

$$\mathbf{S} = \begin{pmatrix} S_0 \\ S_1 \\ S_2 \\ S_3 \end{pmatrix} = \begin{pmatrix} \text{Total Intensity} \\ \text{Horizontal Linear} - \text{Vertical Linear} \\ 45^\circ\ \text{Linear} - 135^\circ\ \text{Linear} \\ \text{Right Circular} - \text{Left Circular} \end{pmatrix} \quad (1)$$

represents the intensity [W/m^2] and polarization state of incident or exitant light. By default, Stokes vectors are column vectors. The Stokes parameters must always satisfy the equation $S_0 \geq \sqrt{S_1^2 + S_1^2 + S_3^2}$. The degree of polarization (DOP) of a Stokes vector,

$$\mathrm{DOP}(\mathbf{S}) = \frac{\sqrt{S_1^2 + S_1^2 + S_3^2}}{S_0}, \tag{2}$$

is a measure of how much of the light under observation is polarized. A DOP of one represents fully polarized light, and a DOP of zero represents fully unpolarized light.

This work uses DOLP

$$\mathrm{DOLP}(\mathbf{S}) = \frac{\sqrt{S_1^2 + S_2^2}}{S_0} \tag{3}$$

and angle of linear polarization (AOLP)

$$\mathrm{AOLP}(\mathbf{S}) = \frac{1}{2}\arctan\left(\frac{S_2}{S_1}\right) \tag{4}$$

to evaluate the linear polarimetric accuracy of metagratings. DOCP

$$\mathrm{DOCP} = S_3/S_0 \tag{5}$$

is used as a complementary polarization parameter in conjunction with DOLP and AOLP to express the full Stokes accuracy. DOLP, AOLP, and DOCP are another way to cast the S_1, S_2, and S_3 Stokes parameters into geometrically intuitive scalar representations.

3. POLARIZATION IMAGING WITH A METASURFACE GRATING–BASIC TECHNIQUE AND DEFINITIONS

The metasurface devices considered here comprise arrays of dielectric pillar-like elements with two axes of mirror symmetry. Each pillar of the array alone can be understood to act in a manner akin to a birefringent wave plate [34,35] whose retardance and overall phase shift can be adjusted by modifying its dimensions and whose fast axis can be adjusted by a rotation of the element itself. In this way, a metasurface serves as an optical element enacting a customizable polarization transformation (encapsulated by a Jones matrix) at each spatial location; by engineering the local transformation enacted by the metasurface at each point, the far field of the device may also be imbued with customized polarization behavior using design methods described extensively elsewhere [12,36,37].

Specializing to the case of diffraction gratings (that is, optical elements in which the pillar-like elements are arranged into periodically repeating unit cells), it is possible to concentrate power into a finite set of diffraction orders while constraining these diffraction orders to act as analyzers for an arbitrarily selected set of polarization states. In other words, using design techniques described extensively in prior work [12], it is possible to design gratings that divide light among a set of diffraction orders according to its polarization state, as though each of these orders were a polarizer for a polarization state specified by the designer.

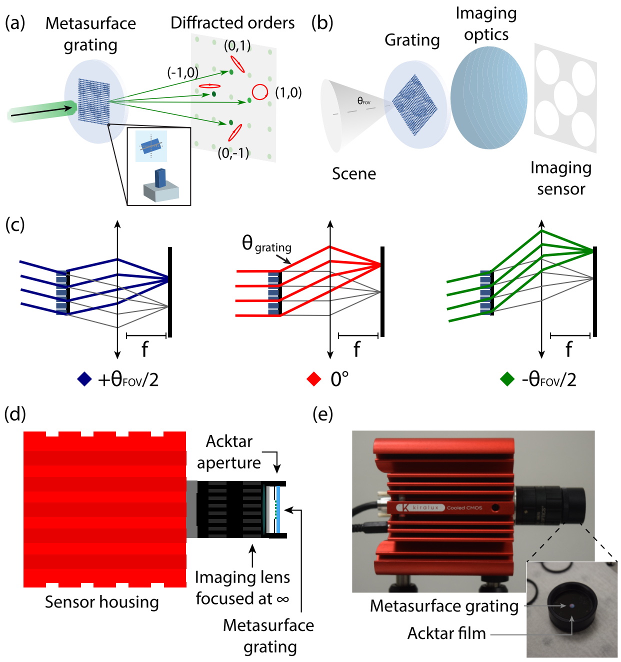

Fig. 1. Polarization imaging through a metasurface polarization grating: concept. (a) A metasurface grating can be designed with orders acting as analyzers for a custom-specified set of polarization states [12]; measuring the power of these diffraction orders provides sufficient information to characterize light's full polarization state. (b) Pairing such a grating with imaging optics permits full Stokes polarization *imaging*. If the grating is turned 45° so that its orders align with the sensor axes, four images will be formed that when registered and inverted using a calibration [Eq. (8)] yield the full Stokes vector over a field of view (FOV). (c) By designing the grating angle $\theta_{\mathrm{grating}}$ to equal this desired FOV, overlap of the polarimetric channels on the sensor can be avoided [13]. (d) Schematic of the example metasurface-based polarimetric imaging system of this work. A conventional infinite conjugate system consisting of a DC-cooled CMOS sensor (Thorlabs part no. CC505MU) is paired with a C-mount machine vision objective ($f = 16$ mm), similar in spirit to [13]. The metasurface is placed at the front face of the lens assembly atop a circular light-absorbing Acktar aperture that assures all light in the system passes through the grating. (e) Photo of the same.

Such a grating, with photodiodes centered on these diffraction orders, could itself serve as the sole optical component in a full Stokes polarimeter suitable for the characterization of, e.g., a beam of collimated laser light, the situation depicted in Fig. 1(a).

The polarizer-like behavior of each diffraction order n of the grating is described by its four-element analyzer vector $\vec{D}_n$. $\vec{D}_n$ for each order specifies several important quantities, namely, the (relative) efficiency of the order (given by its first element), the polarization for which the order analyzes (given by a normalized vector containing the last three elements of $\vec{D}_n$, the "state-of-polarization," which describes the polarization ellipse), and the order's diattenuation [the extent to which the order extinguishes light orthogonal to its preferred polarization state, given by $\mathrm{DOP}(\vec{D}_n)$, cf. Eq. (2)]. Figure 1(a) depicts the four innermost orders of the grating used as polarization state analyzers in this work. These orders are indexed by their Cartesian coordinates as $n \in \{(0, -1), (0, 1), (1, 0), (-1, 0)\}$. Their analyzer vectors $\vec{D}_n$ can be grouped into a 4×4 matrix given as

$$\mathbf{W} = \left[\vec{\mathrm{D}}_{(0,1)}, \vec{\mathrm{D}}_{(1,0)}, \vec{\mathrm{D}}_{(0,-1)}, \vec{\mathrm{D}}_{(-1,0)}\right]^T, \tag{6}$$

which has $\{\vec{\mathrm{D}}_n\}$ as its columns. $\mathbf{W}$ is known as the "polarimetric measurement matrix," and in practice, it (along with $\{\vec{\mathrm{D}}_n\}$) is determined experimentally by a calibration procedure. Two calibration procedures for the present work are developed in Section 5.

If a collimated beam of light, e.g., from a laser, with a polarization state described by the Stokes vector $\mathbf{S}_{\mathrm{inc}}$ is incident on the metasurface grating, it will evoke an intensity I_n on each order n. If these are measured and assembled into a vector $\vec{I}$ whose elements match the ordering of the rows of Eq. (6), we can write

$$\vec{I} = \mathbf{WS} \tag{7}$$

or equivalently,

$$\mathbf{S} = \mathbf{W}^{-1}\vec{I}. \tag{8}$$

If the power directed into each diffraction order is measured and a calibration has been performed, the metasurface grating can serve as the sole polarization component necessary to determine an incident beam's full Stokes vector.

When paired with imaging optics (i.e., a lens), a metasurface polarization grating can be used to construct an imaging polarimeter [Fig. 1(b)]. If we imagine that light from a faraway object is incident on the grating from a range of angles, four images corresponding to the four diffraction orders of interest will be formed, each analyzed with respect to the order's characteristic polarization state. These four images can be registered, and Eq. (8) can, given a pixel-wise calibration of the matrix $\mathbf{W}$ across the field of view (FOV), be applied to the image at each pixel yielding $\mathbf{S}$ at every point (viewing angle) in the photographic scene.

Several design considerations govern the pairing of the grating and imaging optics to measure full Stokes polarization images, considerations that are described in more detail in [13]. The most salient point here is that for the inversion described by Eq. (8) to remain valid, the images formed by individual orders should not be allowed to overlap but should still fully use the available sensor space by just touching. The former constraint means that when imaging a naturally illuminated scene in which light can be incident from any viewing angle, the grating must be preceded by a field stop that limits incident light to a FOV given by θ_{FOV}. The latter constraint implies that, given a desired FOV, the grating's first-order deflection angle θ_g should be selected to be equal θ_{FOV}. This geometrical constraint is illustrated by Fig. 1(b).

If the metasurface grating has a period of length D, as a consequence of the Bragg condition, its first-order angle θ_g is given by

$$\theta_g = \arcsin\frac{\lambda}{D}, \tag{9}$$

where λ is the wavelength of incident light. In other words, the choice of a desired FOV and operating wavelength constrains the grating's period by Eq. (9).

4. DESCRIPTION OF CAMERA UNDER TEST AND THREE SAMPLES USED

The demonstration polarization imaging system studied here [sketched in Fig. 1(d) and pictured in Fig. 1(e)] consists of a metasurface grating placed against the front lens element of a compound camera objective focused at infinity. The objective used here is the same as in [13], a C-mount lens having $f = 16$ mm and an aperture of $f/1.6$ when wide open (Edmund Optics, part no. 59-870). As in [13], the FOV over which polarimetry is conducted is equal to $\theta_{\mathrm{FOV}} \sim 6°$. No field-limiting aperture is required here since the light source in the experiments that follow can be made distant enough not to overfill the desired FOV.

In what follows, we seek to demonstrate robust polarimetric accuracy across the visible spectrum. However, as constructed here, 2D imaging polarimetry is possible only with the metasurface grating within a single narrow wavelength band at a time. Otherwise, due to the grating angle's inherent chromatic dispersion, spatial and polarimetric information for different wavelengths would mix together in a way that does not permit their disambiguation. (However, using modified designs, this constraint can be relaxed and metasurface-based systems for spectropolarimetry can be imagined; see the supplement to [13]).

Given the chromatic dependence of Eq. (9), the grating period must vary if a given grating angle is to be maintained between different wavelength bands. In this work, then, accuracy studies are carried out for different wavelengths by use of different grating samples, effectively creating a different imaging polarimeter by exchange of the sample for tests at different wavelengths. Monochromatic illumination is enforced with bandpass filters throughout the work described in the following sections.

Three gratings are designed here for narrow bands centered on $\lambda = 460$ nm ("blue"), 532 nm ("green"), and 670 nm ("red"). With $\theta_{\mathrm{FOV}} \sim 6°$, the grating period D required in each case is set by Eq. (9). We have $D = Nd$, with N the number of metasurface phase-shifting elements comprising one side of the grating period and d the inter-element separation, each chosen to realize the correct D. The samples are designed using the procedure of [12] and consist of TiO_2 structures whose fabrication has been described thoroughly elsewhere [38]. The design of each grating's periodically repeating unit cell—both as a drawing and as a scanning electron micrograph (SEM)—is shown in Fig. 2 with a uniform 1 μm scale bar.

5. CALIBRATION OF A METAGRATING POLARIZATION CAMERA

The Stokes states analyzed by each diffraction order must be experimentally determined before the metagrating camera can be operated as a linear or full Stokes imaging polarimeter. This section describes two experimental protocols and setups that can be used for determining either the linear or full Stokes states analyzed by a given metagrating camera system, thus calibrating the camera to measure linear or full Stokes vectors of incident light over a FOV. Images assessing the quality of both the linear

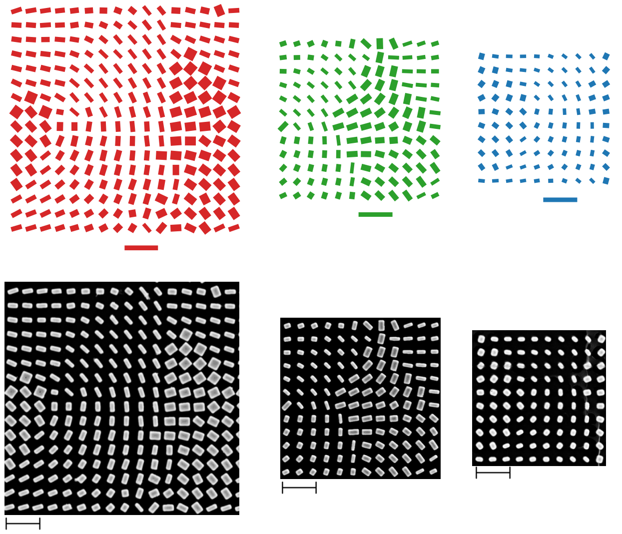

Fig. 2. Intended designs (top) and scanning electron micrographs (SEMs, bottom) of the three metasurface polarization gratings studied in this work. From left to right, these are intended for operation at 670, 550, and 460 nm, respectively. The grating period D varies to keep a constant deflection angle for each wavelength. Each scale bar indicates 1 µm length. In this work, each of these gratings is evaluated using 670 ± 5 nm, 532 ± 1.5 nm, and 460 ± 5 nm illumination, respectively.

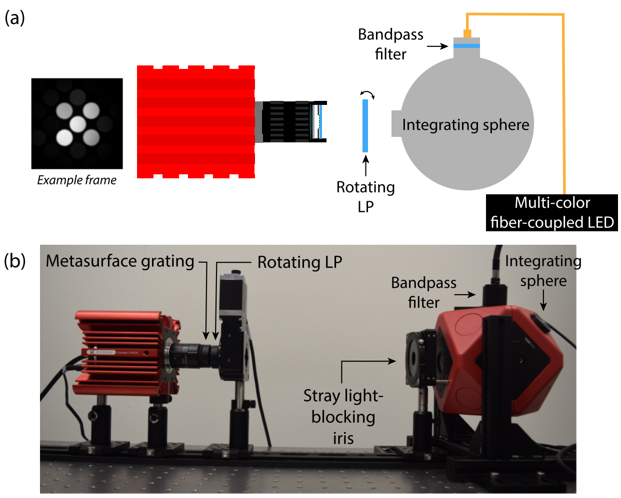

Fig. 3. Calibration setup for linear-only Stokes polarimetry with a metasurface-based imaging polarimeter [(a) schematic and (b) in-lab photograph]. The camera stares through a rotatable linear polarizer into the entrance port of an integrating sphere fed by a wavelength-selectable LED. The simplicity of this setup eliminates hard to calibrate polarization artifacts induced by, e.g., refractive imaging optics. In experimental practice various strategies such as the placement of irises are undertaken to control stray light in the final image.

Stokes and full Stokes calibrations used in this work are provided in Section 3.A and 4.B of Supplement 1, respectively.

A. Linear Stokes Calibration

The linear Stokes vector (that is, the first three Stokes parameters) analyzed by each of the first orders is measured by imaging

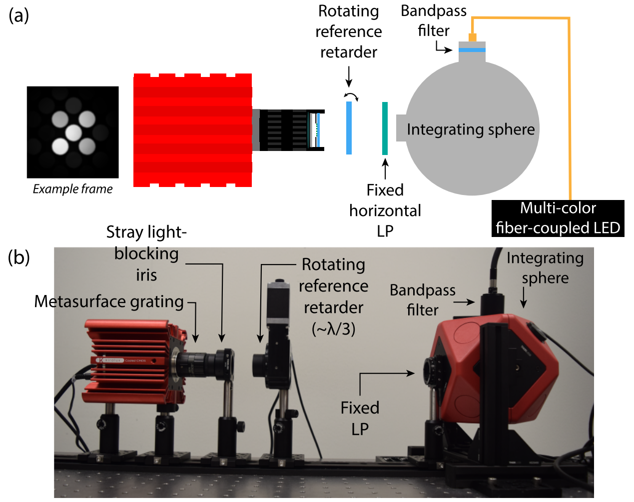

Fig. 4. Calibration setup for full Stokes measurements. [(a) schematic and (b) in-lab photograph]. Light from the integrating sphere passes through a fixed horizontal polarizer and a rotating, pre-characterized retarder (roughly 1/3 wave), thus producing known variable polarization states. As in Fig. 3, several practical steps are taken to control stray light in the final image from the setup itself, including the insertion of an aperture.

the exit port of an integrating sphere source through a rotating linear polarizer $\mathbf{LP}(\theta)$ from $\theta = 0$ to 360° [deg] over 50 steps. Figure 3 depicts the linear-only calibration setup [schematic in (a), photo in (b)]. The metagrating's substrate is mounted into a lens tube with the grating structure facing toward the illumination source. Behind the metagrating is a 3 mm diameter circular aperture used to limit the light that ultimately strikes the detector to only that sorted by the metagrating. The lens tube is attached to the aforementioned $f = 16$ mm camera objective lens that is set to focus at infinity.

The images obtained in this calibration, as well as in all measurements that follow, are corrected for sensor non-uniformities (see the flat fielding procedure described in Appendix A). The polarization analyzing first orders are isolated into $X \times Y$ pixel regions of interest (ROIs) about each order and aligned within a 1/4 pixel accuracy using numerical cross-correlation (as implemented with *phase_cross_correlation()* [39] from scikit-image version 1.7.1 [40]). Appendix B.3 describes an alignment procedure that was empirically found to maximize polarimetric accuracy while minimizing polarization artifacts in the metagrating camera image. Without sub-pixel registration, translations of the diffraction orders across the sensor that arise from rotation of various retarders and polarizer will produce a blurrier image with polarization artifacts.

At each pixel, the set of irradiance images is fit to

$$I(\theta) = a + b\cos(\theta) + c\sin(\theta) + d\cos(2\theta) + e\sin(2\theta), \tag{10}$$

where $I(\theta)$ is the measured intensity, θ is the orientation of the rotating linear polarizer's transmission axis, a corresponds to S_0, b and c fit to systematic errors that do not originate from Malus's law (e.g., effects such as wedges that repeat only after a full 360°), and d and e correspond to S_1 and S_2 of the Stokes parameters, respectively [30]. The AOLP [Eq. (4)] and DOLP [Eq. (3)] image for each diffracted first order's analyzed state is calculated from these fit values. These states form the polarimetric measurement matrix $\mathbf{W}_{\text{Lin}}$, an $N \times 3$ matrix where each row corresponds to the Stokes parameters $\{S_0, S_1, S_2\}$ of the analyzed state by each nth order. In our system, $N = 4$ for each diffracted first order: (0,1); (1,0); (0, −1); and (−1, 0). The final calibration defines a polarimetric measurement matrix $\mathbf{W}_{\text{Lin}}$ for each pixel (x, y) in the larger $X \times Y$ ROI. In this work, the ROI is defined over a 400 × 400 pixel image. The reported accuracy values in Section 6.B are calculated from a smaller circular sub-region within this 400 × 400 ROI, which is illuminated by the integrating sphere source. Polarimetric accuracy is assessed here using normalized metrics such as the DOLP and AOLP; thus, this work first handles intensity values as reported by the camera sensor using "camera units" expressed as 16-bit integers. Accuracy comparisons are drawn from DOLP and AOLP values calculated from normalized, unitless relative intensity images. The particular sensor used in this work outputs images to a 12-bit precision.

B. Full Stokes Calibration

In comparison to the above linear-only calibration, a full Stokes calibration (Fig. 4) is a two-step process that requires the addition of a rotation-stage-mounted retarder (i.e., wave plate). A retardance magnitude between 127° and 132° is suggested for any retarder component that may analyze or generate polarization states in a full Stokes or Mueller rotating retarder polarimeter. The lower bound magnitude of 127° corresponds to an optimized condition number for a rotating retarder Mueller polarimeter's polarimetric measurement matrix [41]. The upper bound magnitude of 132° for a retarder—when paired with a linear polarizer—can be rotated to generate a state that can trace a path that coincides with the points of a normal tetrahedron inscribed in the Poincaré sphere [42]. This work uses an approximately $\lambda/3$ magnitude retarder (close to these mathematical optima) paired with a linear polarizer to perform the full Stokes calibration and reference measurement steps of accuracy evaluation. Our procedure outlined here could also be performed using a $\lambda/4$ retarder if a retarder within the aforementioned range is not available.

1. Retarder Calibration

Our full Stokes calibration starts with measuring the exact retardance magnitude δ of a rotating calibration retarder with Mueller matrix $\mathbf{LR}(\delta, \theta)$ so that it can be subsequently used to calibrate the metasurface-based polarimeter. This is performed by fitting retardance magnitude δ, retarder fast axis orientation offset θ_{LR}, and linear polarizer transmission axis orientation offset θ_{LP} over a series of $L = 100$ irradiance measurements, described by

$$I(r, \theta_{\text{l}}) = \mathbf{LP}(r\theta_{\text{l}} + \theta_{\text{LP}})_{(0,:)}\mathbf{LR}(\delta, \theta_{\text{l}} + \theta_{\text{LR}})\mathbf{LP}(0^\circ) \times (I_0, 0, 0, 0)^T. \tag{11}$$

The retarder is placed between a fixed linear polarizer $\mathbf{LP}(0^\circ)$ and a rotating linear polarizer $\mathbf{LP}(\theta)$. The fixed linear polarizer determines the horizontal $\theta = 0^{\circ\circ}$ orientation of the system. The fast axis offset θ_{LR} and transmission axis offset θ_{LP} values are determined with respect to the first linear polarizer's coordinate system. Incident light $(I_0, 0, 0, 0)^T$ is treated as unpolarized when exiting an integrating sphere source. In this work, the retarder is driven to $L = 100$ positions in $\Delta\theta = 3.63^\circ$ steps. The linear polarizer is spun in tandem with the retarder at a ratio of $r = 2.5$, an optimized value that is sensitive to $\frac{\pi}{4} \leq \delta \leq \frac{\pi}{2}$ retardance magnitudes without being sensitive to θ_{LP} and θ_{LR} offset angles. Appendix C explains how this ratio was chosen.

Equation (11) can be simplified to

$$I(r, \theta_{\text{l}}) = \vec{\text{A}}_{\text{LP}}(r\theta_{\text{l}} + \theta_{\text{LP}}) \cdot \vec{\text{G}}(\theta_{\text{l}} + \theta_{\text{LR}}, \delta), \tag{12}$$

where $\vec{\text{A}}_{\text{LP}}$ is the 1 × 4 polarization state analyzer vector

$$\vec{\text{A}}_{\text{LP}}(\theta) = [\mathbf{LP}(\theta)]_{(0,:)} = \frac{1}{2}(1, \cos(2\theta), -\sin(2\theta), 0), \tag{13}$$

equivalent to the Stokes vector described by the top row of the Mueller matrix of an arbitrarily rotated linear polarizer, and $\vec{\text{G}}$ is the polarization state generator vector

$$\vec{\text{G}}(\theta, \delta) = \mathbf{LR}(\delta, \theta)\mathbf{LP}(0)(I_0, 0, 0, 0)^T. \tag{14}$$

2. Instrument Calibration

The second step in this full Stokes calibration procedure measures the full Stokes polarization state analyzed by each diffracted order. The rotating linear polarizer is removed from the previous characterization setup, and the metagrating is inserted before the camera objective as shown in Fig. 3. A series of L irradiance measurements is captured using the newly characterized retarder

$$I_{n,l}(\theta_l, \delta) = \vec{\text{D}}_n \cdot \vec{\text{G}}(\theta_l + \theta_{\text{LP}}, \delta), \tag{15}$$

where n indicates the order that this irradiance measurement belongs to, and l corresponds to the position in the sequence of L irradiance measurements: $\vec{\text{I}}$. We then rotate the retarder over $L = 50$ positions from $\theta_{l=0} = 0$ to $\theta_{l=50} = 360^\circ$ in uniform steps of $\Delta\theta_l = 7.34^\circ$]. Equation (15) replaces the rotating linear polarizer in Eq. (10) with the unknown analyzed Stokes state corresponding to the nth diffraction order in the metagrating camera, $\vec{\text{D}}_n$. Equation (15) replaces the unknown incident Stokes vector $\mathbf{S}$ with $\mathbf{G}$, a matrix of generated states that can be calculated using Eq. (14). In other words, the calibrated retarder is rotated to produce a number of polarization states that can be calculated and taken as known (these form the columns of $\mathbf{G}$), which can then be used to calibrate the metasurface polarimeter.

Each diffracted order's $\vec{\text{D}}_n$ is determined using

$$\vec{\text{D}}_n = \vec{I}_n\mathbf{G}^{-1}, \tag{16}$$

where $\vec{I}_n$ is a series of irradiance measurements by the nth order formed as an L-element list. The full Stokes calibration for a metagrating camera is the $N \times 4$ polarimetric measurement matrix $\mathbf{W}_{\text{FS}}$, where each column is an analyzer vector $\vec{\text{D}}_n$.

Here we treat the retarder $\mathbf{LR}$ as a pure retarder that is uniform across its entire aperture. Retarders often vary in magnitude over their clear aperture. Accounting for these variations would require a pixelwise measurement of retardance magnitudes. Applying this map over a series of rotating retarder positions requires the map to be either digitally rotated or empirically measured at each rotation position—an effort that we do not attempt in this work.

The full Stokes calibration produced at the end of this procedure is defined as an $X \times Y$ pixel ROI where each pixel is defined by an polarimetric measurement matrix, $\mathbf{W}_{\mathrm{FS}}$. This $\mathbf{W}_{\mathrm{FS}}$ is applied to $X \times Y$ quadrant images $\vec{I}_n$ pulled from the same pixels the polarimetric measurement matrix is calculated from and treated with the same sub-pixel alignment that was used. The reported accuracy values in Section 6.C are calculated from a smaller circular sub-region within this 400×400 ROI, which is illuminated by the integrating sphere source.

6. ACCURACY STUDY

A. General Problem

Once calibrated, individual quadrant images acquired by the metagrating camera can be registered and consolidated into a pixelwise measurement of the Stokes vector by Eq. (8). In this section, we assess the accuracy of this aggregate measurement process (the acquired calibration and associated image registration/reduction) through comparison to reference measurements.

The reference measurements used here are acquired by two division-of-time polarimeters (the first linear-only, and the second full Stokes) constructed from traditional polarization optics. Highly accurate division-of-time polarimetry relies on the assumption that the observed subject is motionless over the measurement time window. The division-of-time method is therefore unsuited to problems where a subject is in motion relative to the camera's position. However, division-of-time measurements are suitable for a laboratory setting as a ground truth reference measurement that may be compared to results from a metagrating polarimeter under study. This section uses division-of-time methods implemented across 50 (for linear-only) or 16 (for full Stokes) frames as reference measurements. In the linear case, the reference measurement uses the assumption that a linear polarizer is a pure polarizer at its foundation; in the full Stokes case, this assumption is augmented with the assumption of perfect knowledge of a retarder whose parameters have been characterized as described in Section 5.B.

These references are compared to the metagrating's division-of-amplitude method, in which one FOV is split into four ROIs. All images are captured using frame averaging to reduce random noise effects from the sensor, effectively producing a study that probes at the ability to calibrate and retrieve accurate results from a metasurface-based polarimeter.

B. Linear Stokes Accuracy

Linear Stokes accuracy is evaluated here through comparing each polarimeter's ability to measure the DOLP and AOLP of a measurement subject. We make use of the tilted glass plate method described in [23,30], which enables simultaneous assessment of DOLP and AOLP accuracy by utilizing simple Fresnel transmission and reflection as a glass plate is progressively tilted after a monochromatic illumination source to experience normal to oblique incident illumination. Figures 5(a)–5(d) depict the mounting apparatus that varies DOLP by tilting the plane-parallel plate to plate angle θ_p and varies AOLP by rotating the cradle in which the plate is mounted to cradle angle θ_c. The linear Stokes state generated by the tilted plate can be estimated using

$$\vec{S}_{\mathrm{Lin}}(\theta_{\mathrm{p}}, \theta_{\mathrm{c}}) = \frac{1}{2}\left(\begin{array}{c} T_s + T_p \\ (T_s - T_p)\cos(2\theta_{\mathrm{c}}) \\ -(T_s - T_p)\sin(2\theta_{\mathrm{c}}) \end{array}\right), \tag{17}$$

where $T_s = |t_s(\theta_{\mathrm{p}})|^2$ and $T_p = |t_p(\theta_{\mathrm{p}})|^2$ are the intensities of transmitted s-polarized and p-polarized light calculated using Fresnel transmission through a plane-parallel plate of index n_{plate} in air. Equation (17) is an intuitive, overly simplified expression of the Fresnel transmission taking place by treating the real-world experiment instead as a single transmission event. The linear polarization accuracy experiment does not require a $\vec{S}_{\mathrm{Lin}}$ calculated from n_{plate}. Instead, this linear polarization accuracy experiment compares the *reference* linear Stokes image as measured by a rotating linear polarizer to the *validation* linear Stokes image as measured by the metagrating polarimeter.

In this work, the glass plate is tilted from $\theta_{\mathrm{p}} = -60$ to $60°$ in $\Delta\theta_{\mathrm{p}} = 15°$ steps to vary DOLP. The cradle mount is rotated from $\theta_{\mathrm{c}} = 0$ to $180°$ in $\Delta\theta_{\mathrm{c}} = 45°$ steps to vary AOLP. Linear stokes accuracy is evaluated over a total of 45 plate orientations and by assessing the average and standard deviation of $\Delta\mathrm{DOLP} = \mathrm{DOLP}_{\mathrm{Ref}} - \mathrm{DOLP}_{\mathrm{Val}}$ and $\Delta\mathrm{AOLP} = \mathrm{AOLP}_{\mathrm{Ref}} - \mathrm{AOLP}_{\mathrm{Val}}$.

For the validation measurement, the metagrating camera is operated as a division-of-amplitude polarimeter. A validation measurement is described by the four-element list of irradiances

$$\vec{\mathrm{I}}_{\mathrm{Lin\,Val}}(\theta_{\mathrm{p}}, \theta_{\mathrm{c}}) = \mathbf{W}_{\mathrm{Lin}}\vec{S}_{\mathrm{Lin}}(\theta_{\mathrm{p}}, \theta_{\mathrm{c}}), \tag{18}$$

where each element of the vector corresponds to one diffraction order. $\mathbf{W}_{\mathrm{Lin}}$ is the polarimetric measurement matrix of the metagrating determined through linear Stokes calibration described in Section 5.A. Linear Stokes images are calculated from these validation images by applying

$$\vec{S}_{\mathrm{Lin\,Val}}(\theta_c, \theta_p) = \mathbf{W}_{\mathrm{Lin}}\vec{\mathrm{I}}_{\mathrm{Lin\,Val}}(\theta_c, \theta_p) \tag{19}$$

in a pixelwise manner. Figures 5(e) and 5(f) depict the validation measurement setup.

The reference linear Stokes vector is measured by rotating a linear polarizer through a series of $L = 50$ transmission axis positions spanning from $\theta_l = 0$ to $360°$ in $\Delta\theta_l = 3.63°$ steps. An irradiance measurement,

$$\vec{\mathrm{I}}_{\mathrm{Lin\,Ref}}(\theta_{\mathrm{p}}, \theta_{\mathrm{c}}, \theta_l) = \mathbf{LP}(\theta_l)\vec{S}_{\mathrm{Lin}}(\theta_{\mathrm{p}}, \theta_{\mathrm{c}}), \tag{20}$$

is collected for each combination of plate and cradle position. The reference Stokes parameters, $\vec{S}_{\mathrm{Lin\,Ref}}(\theta_{\mathrm{p}}, \theta_{\mathrm{c}})$, are then calculated by curve fitting Eq. (10) to the list of $L = 50$ irradiance measurements $\vec{\mathrm{I}}_{\mathrm{Lin\,Ref}}(\theta_{\mathrm{p}}, \theta_{\mathrm{c}}, \{\theta_l\})$. The reference measurements repeat the same procedure used to establish a linear Stokes calibration on the metagrating. Figures 5(e) and 5(g) depict the reference measurement setup. The validation and reference camera setups are nearly identical with the exception of the removal of the metagrating and insertion of a rotating linear polarizer. An important point here is that the aperture used as a backing for the metasurface grating during the validation

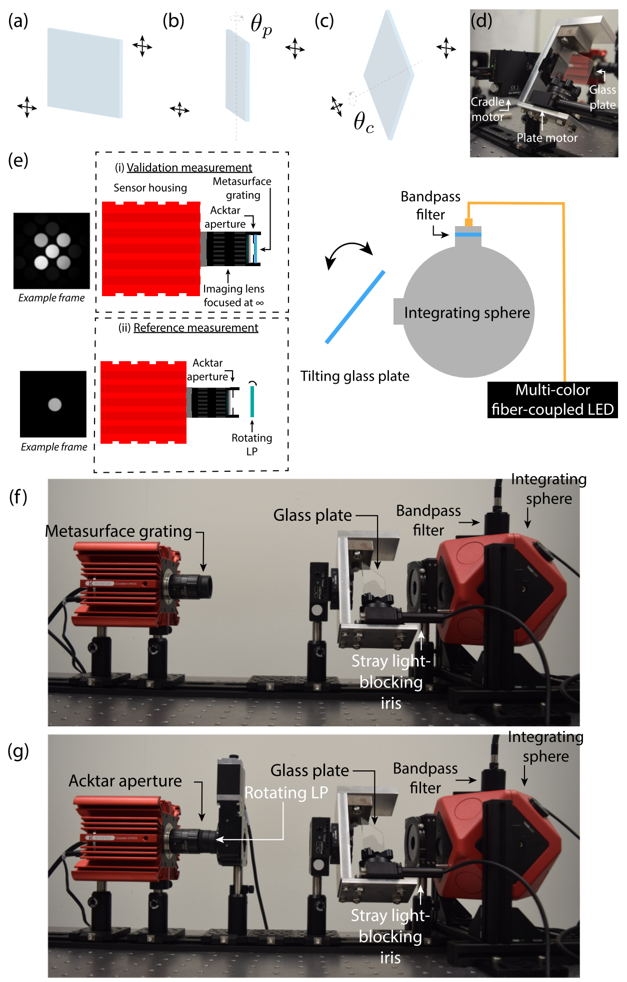

Fig. 5. Linear polarization accuracy study with a metasurface-based imaging polarimeter. The basis of the accuracy study is a tilting glass plate that, due to Fresnel interaction, can render initially unpolarized light (e.g., from an integrating sphere) controllably partially polarized. (a) At normal incidence, the light remains unpolarized and (b) becomes preferentially s polarized at an angle. We refer to this as the plate angle θ_p. (c) The plate can also be rotated about its axis on a cradle, changing the axis of linear polarization; we refer to this as cradle angle θ_c. Both θ_p and θ_c can be controlled independently with an appropriate mount as in (d). (e) The tilting plate is illuminated by light from an integrating sphere and imaged by the camera, (i) first in a validation measurement through the metasurface grating and (ii) in a reference measurement through the same camera, instead through a rotating polarizer with the metasurface grating removed. The validation measurement set up is shown in (f) and the reference in (g).

measurement is left in place during the reference measurement; this way, the camera's entrance pupil (EP) size and location are left constant, so that the reference and validation cameras are actually observing under identical conditions and can be compared. Great care is taken not to move the camera during this exchange between validation and reference to assure the same; we find that the sub-percent accuracy in DOLP sought here can easily be disturbed by slight differences in observing conditions between reference and validation.

Each reference and validation measurement averages 100 frames to minimize the effects of random readout noise in the sensor. The appropriate flat field profile corresponding to the wavelength and exposure time of the validation measurement is applied to the data to account for structured noise effects described in Appendix A. $\vec{\mathrm{I}}_{\mathrm{Lin\,Val}}(\theta_\mathrm{p}, \theta_\mathrm{c})$ and $\vec{\mathrm{I}}_{\mathrm{Lin\,Ref}}(\theta_\mathrm{p}, \theta_\mathrm{c})$ are flat field corrected irradiances.

The resulting DOLP and AOLP values are compared to a reference measurement set at the same plate positions. These reference values are captured by replacing the metagrating with a rotating linear polarizer. The 50 reference images taken over linear polarizer orientations from 0° to 360° are fit using Eq. (10) to retrieve the linear Stokes parameters. Figure 5 depicts these validation and reference measurement setups for this linear Stokes accuracy test.

The positions at $\theta_\mathrm{p} > 0°$ and $\theta_\mathrm{c} = 0°$ are mirrored to the $\theta_\mathrm{p} < 0°$ positions at $\theta_\mathrm{c} = 360°$. Variations across $\theta_\mathrm{p} = 0°$ can be partly attributed to low DOLP scattering from planar surfaces in the surrounding real-world laboratory environment. Collecting seemingly redundant data at $\theta_\mathrm{c} = 180°$ serves to disambiguate systematic effects in the metagrating camera from effects in the real-world laboratory.

DOLP and AOLP are calculated from the reference and validation linear Stokes images using Eqs. (3) and (4). The residual values $\Delta\mathrm{DOLP} = \mathrm{DOLP}_{\mathrm{Ref}} - \mathrm{DOLP}_{\mathrm{Val}}$ and $\Delta\mathrm{AOLP} = \mathrm{AOLP}_{\mathrm{Ref}} - \mathrm{AOLP}_{\mathrm{Val}}$ assess the metagrating's linear Stokes accuracy.

Figure 6 depicts both reference and validation DOLP and AOLP for a glass plate oriented at $\theta_\mathrm{p} = -60$ and $\theta_\mathrm{c} = 0°$ under 532 nm illumination. A gradient of ± 0.006 DOLP spans across a $\pm 1.56°$ FOV in a pattern consistent with illumination of a tilted plane by a slightly diverging illumination source. This narrow FOV limitation is due to the diameter of the outport of

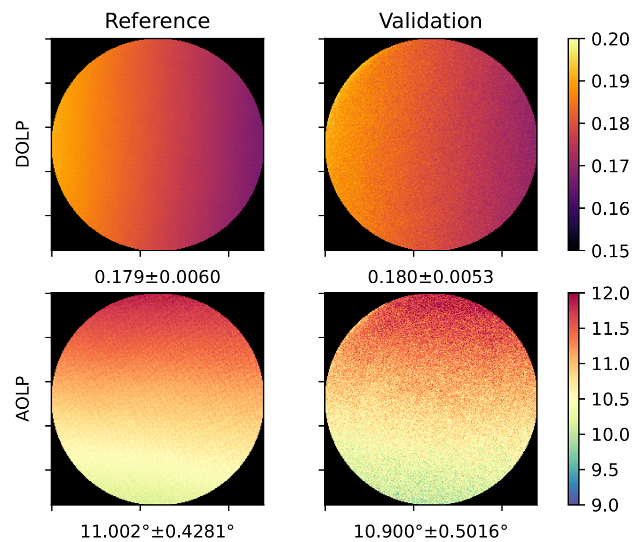

Fig. 6. Degree of linear polarization (DOLP) and angle of linear polarization (AOLP) are compared for cradle position $\theta_c = 0°$ and plate position $\theta_\mathrm{p} = -60°$ linear Stokes accuracy measurement at 670 nm. The reference data are taken by imaging through 50 different linear polarizer positions. The validation data are taken by imaging through a polarization metagrating and using only four analyzing diffraction orders. The region of interest (ROI) depicted above spans a $\pm 1.56°$ field of view in a 240 × 240 pixel image. The numbers below each image indicate the mean and first standard deviation of values within the FOV. The gradient of values across the images is consistent with a diverging light source striking a tilted glass plate.

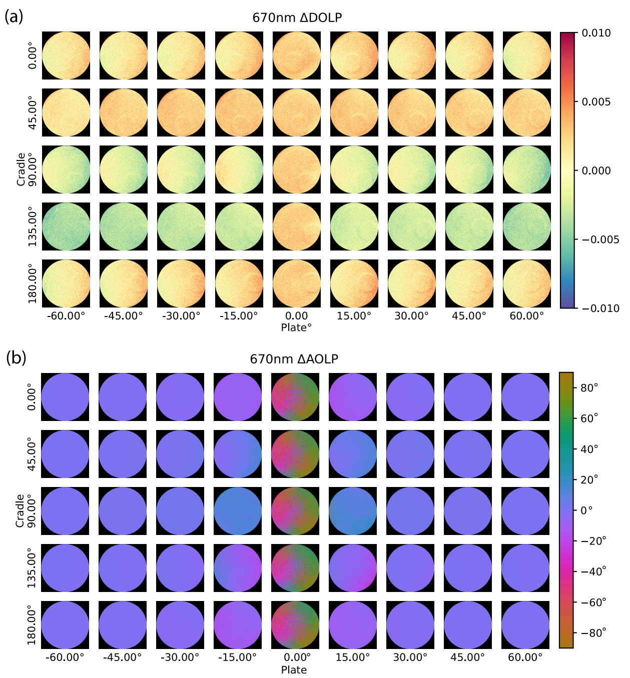

Fig. 7. Residual errors for (a) degree of linear polarization (ΔDOLP) and (b) angle of linear polarization (ΔAOLP) between the reference and validation data. The handedness and magnitude of the ΔDOLP is dependent on the cradle angle θ_c of the tilted plate. Signal to noise ratio for AOLP decreases as the DOLP decreases, leading to an increase in the difference between the validation and reference AOLP images. For metagrating polarimeter measurements of near 0° incident illumination, the AOLP accuracy offset becomes more pronounced. These features are consistent with an increase in uncertainty, as fewer sampling points are used during calculation. See Supplement 1 for the same figure at 460 and 532 nm.

the integrating sphere and the polarizing optics readily available to a benchtop system. An augmented tilted plate experiment with additional opto-mechanics and more reflection artifact management would be required to assess a larger range of angles. In this work, we are limited to DOLP ≤ 0.220 due to the size and refractive index of the single glass plate used during DOLP accuracy evaluation, a range that could similarly be extended with use of more and higher index glass plates.

Figure 7 presents ΔDOLP for the 670 nm linear Stokes dataset. $\Delta\text{DOLP} < 0$ at the $\theta_c = 0°$ plate positions, which indicates that the metagrating measures a higher DOLP in comparison to the reference rotating linear polarizer's measurements. Near $\theta_c = 90°$, the metagrating measures a lower DOLP in comparison to the reference linear polarizer's measurements. At the more acute plate angles $\theta_p = \pm 15°$, ΔDOLP increases due to the numerical offset in the metagrating camera system dominating the signal in the validation data.

Figure 7 depicts the ΔAOLP for the same 670 nm linear Stokes dataset presented in Fig. 7. The plate angles at $\theta_c = 0$ and $\theta_c = 180°$ are mirrored from one another about $\theta_p = 0°$. Across all $\theta_p = 0°$ positions, ΔAOLP has a consistent non-zero pattern across the FOV. Low amounts of partially linearly polarized light—originating from first surface scatter from the Spectralon inside the integrating sphere [43]—are measurable by the rotating polarizer reference procedure, but are not detected by the metagrating. A DOLP offset in the metagrating result is larger than the weak linear polarization signal present at near to normal incidence of $\theta_p = 0$.

Figure 8 is provided as an overlook of the ΔDOLP performance that is formatted in the same tradition as [23,30]. The results from each wavelength are plotted as pointclouds in colors corresponding to each grating's designed wavelength (red for 670 nm, green for 532 nm, and blue for 460 nm). Linear polarization accuracy metrics of these same measurements are summarized in Table 1. The linear Stokes precision is calculated as the standard deviation of the residual between the reference and validation DOLPs. Over all three assessed wavelength designs, the precision of ΔDOLP is within ±0.5%. The standard deviation of ΔDOLP is represented by errorbars in Fig. 8; the spans of these errorbars lie within the ±0.5% DOLP, denoted by the gray region in each plot.

C. Full Stokes Accuracy

This subsection describes the implementation of the circular polarization accuracy experiment designed to complement the tilted plate linear Stokes accuracy test described in Section 6.B. Only the 532 nm metagrating is analyzed in this section. This complementary experiment uses a rotating retarder and fixed linear polarizer as paired test elements instead of a tilted glass plate. This pair is used to create a full Stokes generator described by Eq. (14) that is similar to the generator used for the full Stokes calibration in Section 5.B. However, an off-the-shelf $\lambda/4$ retarder at 532 nm is used to generate the target states during the accuracy test (i.e., $\delta_g = \lambda/4$). The linear polarizer used to generate $\vec{G}$ [Eq. (14)] is identical to the one used in the full Stokes calibration of the metagrating camera. A series of $G = 50$ positions from $\theta_g = 0$ to 360° in $\Delta\theta = 3.63°$ steps are used to assess circular polarization accuracy. This is the same full Stokes state generating method as described in Section 5.B.

Figure 9 shows results from the full Stokes calibration of the 532 nm (green) metagrating, comparing the ellipses of the polarization states analyzed by each grating order to those derived from a full-wave simulation of the design. Deviation between the major axes of the measured and simulated polarization ellipses is partly attributable to rotational ambiguity between the metagrating's orientation as-mounted and the horizontal transmission axis $\mathbf{LP}(0°)$ of the generator. The remaining variation between the measured and simulated states are attributable to the deviation of the final fabricated design from the simulated design. Section 4.A in Supplement 1 presents a few approaches for assessing the quality and accuracy of the measured polarimeter's versus the simulated grating's performance.

Figure 10 depicts the validation and reference measurement setups. Reference measurements are taken using a rotating linear polarizer and a rotating retarder using the test sequence described by

$$I_{\text{FS Ref}}(\theta_g, \theta_a) = \vec{A}(\theta_a) \cdot \vec{G}(\theta_g), \tag{21}$$

where the analyzer vector is

$$\vec{A}(\theta_a) = (\mathbf{LP}(r\theta_a + \theta_{\text{LP}})\mathbf{LR}(\delta_a, \theta_a + \theta_{\text{LR}}))_{[0,:]}, \tag{22}$$

and the generator vector $\vec{G}(\theta_g)$ is the same as Eq. (14).

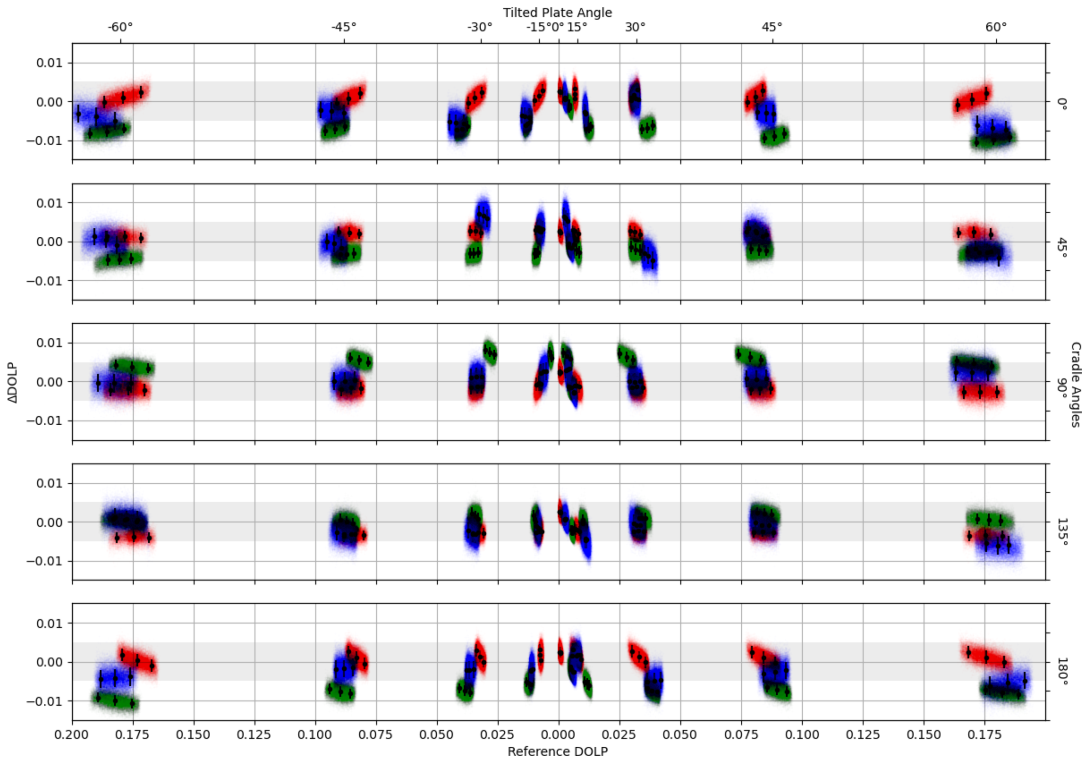

Fig. 8. Difference (ΔDOLP) between the reference DOLP and validation DOLP is plotted versus the reference DOLP for each pixel in the tested region of interest. The lower x-axis labels indicate the reference DOLP value. The upper x-axis labels indicate the tilted plate angle that corresponds to the cluster of plotted pixel values in each plot. The red, green, and blue scattered points correspond to the 670, 532, and 460 nm metagrating samples, respectively. The gray stripe within each plot indicates ±0.5% DOLP error, which is often quoted as the minimum accuracy required to perform aerosol polarimetry.

Table 1. Residual Degree of Linear Polarization (ΔDOLP) in [%] and Residual Angle of Linear Polarization (ΔAOLP) in [°] as Measured by the Tilted Plate Test in Section 6.B[a]

λ [nm]	670 ± 5	532 ± 1.5	460 ± 5
ΔDOLP	0.225 ± 0.149	0.519 ± 0.306	0.331 ± 0.261
ΔAOLP*	3.095 ± 6.561	6.352 ± 15.498	6.627 ± 19.582
ΔAOLP**	1.031 ± 1.043	2.002 ± 1.960	1.350 ± 1.485

[a]Mean and standard deviations over ±1.56° field of view are given for each accuracy metric. Measured AOLP accuracy values at the $\theta_p = 0°$ tilted plate angle are omitted from the ΔAOLP* calculation. ΔAOLP** values omit the $\theta_p = 0°$, ±15° tilted plate measurements from the calculation. This effectively limits the ΔAOLP** measurements to include only $\mathrm{DOLP_{ref}} > 0.02$ data. This diminished precision and accuracy with lower DOLP is not unique to the metagrating polarimeter; it is a consequence of low signal to noise ratio.

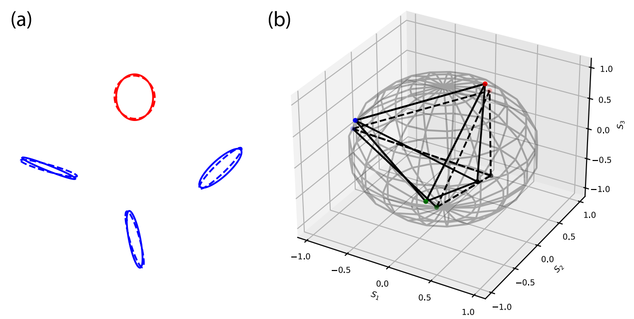

Fig. 9. (a) The polarization ellipses compare the simulated (dashed) Stokes state versus the average measured (solid) Stokes state over the region of interest displayed in Fig. 11. Right circular polarization handedness is indicated by red, while left circular polarization handedness is indicated by blue. An overall rotation in the metagrating's placement is observable in comparing the major axes of the simulated versus measured ellipses; this rotation indicates that the horizontal axis of the metagrating is misaligned to the transmission axis of the first linear polarizer. This rotation affects only the orientation of the measured polarization state, which can be corrected in post-processing. (b) The simulated full Stokes analyzer states are plotted here as opaque circles, while the measured full Stokes analyzer states are plotted as transparent circles. In addition to major axis orientation offset between the ellipses of the analyzed states, the full Stokes calibration states also vary in ellipticity and degree of polarization. The tetrahedron inscribed by the calibration states is both smaller than and deformed in angle for a regular tetrahedron within a unit sphere.

The same $r = 2.5$ rotation ratio used during full Stokes calibration is used here. The $\lambda/3$ analyzer retarder can be the same component used in full Stokes calibration of the metagrating. In this work, a series of $A = 16$ analyzer angles from $\theta_a - 0$ to 360° in $\Delta\theta_a = 22.5°$ steps is used in each reference measurement. The full Stokes state measured by the reference measurement is recovered using

$$\vec{G}_{\mathrm{FS\ Ref}} = \mathbf{A}^{-1}\vec{\mathrm{I}}_{\mathrm{FS\ Ref}}(\theta_g, \vec{\theta}_a), \tag{23}$$

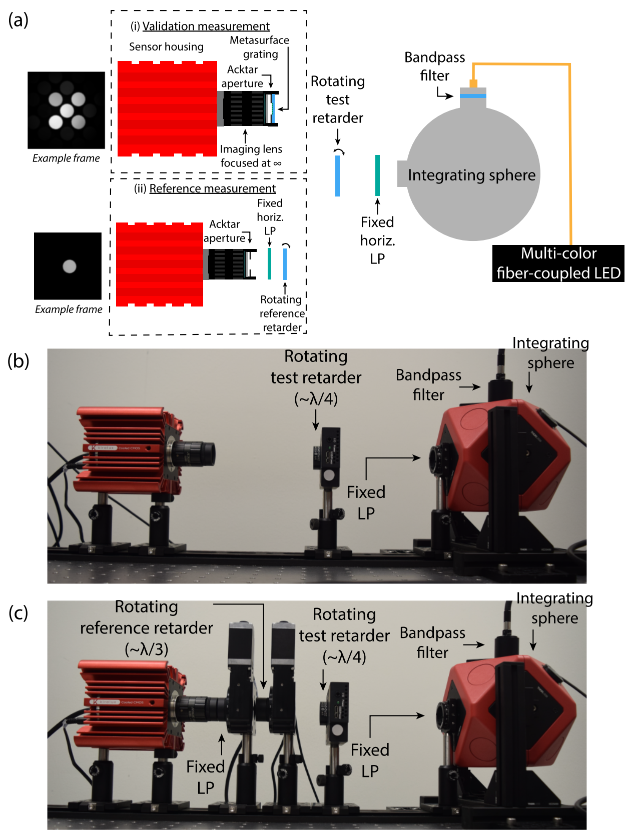

Fig. 10. Full Stokes accuracy study. (a) Light illuminates a rotating retarder through a fixed linear polarizer producing unknown polarization states over the camera FOV. These are imaged first in a validation measurement (i) through the metasurface camera and (ii) repeated through a reference camera that is the same as the validation camera with the metasurface removed and replaced with a polarization analyzer consisting of a characterized rotating retarder and fixed linear polarizer. The full Stokes validation measurement is depicted in (b) and the reference measurement in (c).

where $\vec{\mathrm{I}}(\theta_g, \vec{\theta}_a)$ is a 16×1 vector of irradiances corresponding to the gth test state. The polarimetric measurement matrix for this reference sequence is $\mathbf{A}$, a 16×4 matrix where each row is a full Stokes analyzer vector $\vec{A}(\theta_a)$.

The validation measurement test sequence is described by

$$\vec{\mathrm{I}}_{\mathrm{FS\,Val}}(\theta_g) = \mathbf{W}_{\mathrm{FS}} \vec{G}(\theta_g), \tag{24}$$

which is a recasting of the calibration measurement equation [Eq. (21)]. This 4×1 vector of irradiances is measured by a full Stokes calibration $\mathbf{W}_{\mathrm{FS}}$, the metagrating's polarimetric measurement matrix [Eq. (6)]. Each generated state measured by the metagrating is determined using

$$\vec{G}_{\mathrm{FS\,Val}} = \mathbf{W}_{\mathrm{FS}}^{-1} \vec{\mathrm{I}}_{\mathrm{FS\,Val}}(\theta_g), \tag{25}$$

a recasting of Eq. (8).

The DOCP of the full Stokes state is calculated using Eq. (5). Figure 11 displays seven out of 50 of the full Stokes states measured by both the metagrating camera validation measurement and the rotating linear polarizer and retarder reference measurements. The polarization ellipse measured by the validation setup is plotted with a solid line while the reference ellipses is plotted with a dashed line. Circular polarization accuracy metrics of these same measurements are summarized in Table 2. Circular polarization accuracy tends to become less accurate as the state under analysis becomes more circular. This is due to the specific selection of analyzer states, which favor right-hand elliptical basis states to form $\mathbf{W}_{\mathrm{FS}}$. The analyzed states are spaced as a regular tetrahedron during the design process with a specific choice made during this proof of concept to place one of the vertices at a pole of the Poincaré sphere, as seen in Fig. 9. As a result, the linear states are more accurately measured by the final fabricated metagrating. Any error or noise in the state probing the pole would have an out-sized effect on the accuracy of S_3. This preferential handedness offset is observable in Fig. 11. Using the same process [12], a future grating could be designed to implement a different variant of the tetrahedron states in which all four are elliptical in a way that is balanced between the equator and the poles of the Poincaré sphere.

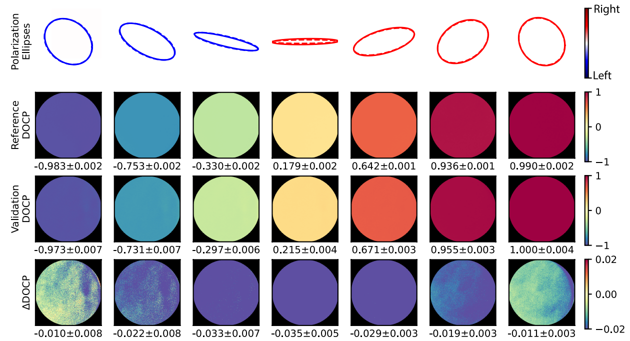

Fig. 11. Top row displays the polarization state measured over the average ROI by the reference (dashed) and validation (solid) measurements for the 532 nm full Stokes test. Right circular polarization handedness is indicated by red, while left circular polarization handedness is indicated by blue. The second row shows the DOCP over the FOV as measured by the rotating reference linear polarizer and analyzer $\lambda/3$ retarder pair. The third row is the DOCP for the same states as measured by the metagrating camera. The last row is the signed difference between reference and validation. Below each FOV are the mean DOCP values $\pm$ the standard deviation of DOCPs inside the FOV. See Supplement 1 for further measurements. Only the 532 nm grating was assessed for full Stokes accuracy. The ROI displayed above spans a $\pm 2°$ FOV in a 290×290 pixel image. A preferential handedness toward $\Delta\mathrm{DOCP} \leq 0$ is demonstrated in both the last row of this figure and in Table 2.

Table 2. DOCP Accuracy (ΔDOCP) Determined by Operating the Metagrating Camera as a Full Stokes Polarimeter[a]

Parameter	$\lvert\Delta\mathrm{DOCP}\rvert$	$\Delta\mathrm{DOCP}$
$\mathrm{DOCP} \leq -0.2$	0.0148 ± 0.0114	-0.0079 ± 0.0169
$0.2 \geq \mathrm{DOCP} > -0.2$	0.0229 ± 0.0145	-0.0138 ± 0.0233
$0.5 \geq \mathrm{DOCP} > 0.2$	0.0221 ± 0.0148	-0.0135 ± 0.0221
$\mathrm{DOCP} > 0.5$	0.0150 ± 0.0098	-0.0145 ± 0.0105
All DOCPs	0.0162 ± 0.0120	-0.0113 ± 0.0167

[a]DOCP accuracy values are binned by the reference DOCP measurement taken by a $\delta = 0.336\lambda$ retarder under 532 ± 1.5 nm illumination. The values calculated here span a $\pm 2.00°$] field of view. At lower DOCP magnitudes, ΔDOCP increases. A preferential handedness toward $\mathrm{DOCP} < 0$, or left circularly polarized light, is observed across the entire set.

7. CONCLUSION

Polarization-sensitive metasurfaces, which can combine the function of many freespace polarization elements into a single optic, have attracted interest as future components in division-of-amplitude polarimetric imaging systems. In this work, we have explicitly considered the precision and accuracy with which this polarimetry can be performed. We performed two studies: the first study assesses the metasurface polarimeter's ability to measure linear polarization, and the second study probes the metasurface polarimeter's ability to measure circular polarization. In both cases, measurements taken by the metasurface-based device were compared to measurements taken with division-of-time benchtop references using traditional polarization optics (i.e., polarizers and retarders) as described throughout the sections above.

The three polarization metagratings tested in this work were designed to operate at 670, 532, and 460 nm. The precision of ΔDOLP is within ±0.3% across the three wavebands tested, and the precision of Δ DOCP is within ±2.4% for the 532 nm grating. In requiring a uniform and polarization-aberration-free ROI, the FOV over which accuracy is reported is limited from ±3 to ±1.56° for linear Stokes analysis and ±2.00° for full Stokes analysis. See Tables 1 and 2 for further accuracy metrics for linear Stokes and full Stokes parameters, respectively.

There are a number of ways in which this work could be improved. In terms of the camera characterization, linear polarization accuracy was studied only for light with DOLP ≤ 0.2 due to the particular index and shape of the glass plate used in the tilted plate test. This range could be extended with an improved setup employing a cascade of multiple plates, each ideally having a high refractive index. Moreover, the full Stokes accuracy study presented could be extended with the inclusion of a tilted plate with the retarder to prepare well-characterized elliptically *partially* polarized light; this would represent the most general accuracy study.

Further improvements to this work are related to the metasurface imaging polarimeter itself. Ideally, the metasurface polarization grating would be placed in a system's aperture stop or a pupil plane [13]. This is not the case here because the stop location is inaccessible in our camera objective. Further improvement in terms of imaging quality and polarimetric accuracy would be expected if the metasurface could be placed at the stop. The placement of the grating in front of the camera may be an asset in some applications, but applications with more specific quantitative requirements (e.g., scientific remote sensing) would ideally use an imaging system designed around the metasurface possessing other desirable qualities such as image-space telecentricity.

Other improvements would center on the gratings. The polarization states analyzed by the grating occupy the vertices of a tetrahedron inscribed in the Poincaré sphere, but the choice of the states that form that tetrahedron is not unique. The metagratings in this work analyze a tetrahedron where one of the analyzed states is purposefully set to a fully circular state (see Fig. 9 and [44], the first work to suggest using this configuration). This results in a situation where linear states of polarization are uniformly sampled, but three of four analyzed states share one handedness ($S_3 < 0$) so the opposite handedness ($S_3 > 0$) is sampled only once. A future design [12] of four analysis states that more equally samples the S_3 component could be modeled after the set of four Stokes states defined in [42].

Finally, the FOV over which polarimetric accuracy was studied by this work was relatively small with a ±1.56° FOV in the linear Stokes test and a ±2.00° FOV in the full Stokes test. This is in part due to the inherent challenge of designing a high FOV polarimetric imaging system based on a metasurface in this way—the grating's deflection angle must scale with the desired FOV [13]. However, characterizing a large FOV metagrating-based camera to the level of accuracy described in this work would pose a measurement challenge as well. Expanding the limit of the analyzed FOV would require either larger clear apertures along the optical path or an approach that stitches together multiple measurements over a full FOV.

Metasurfaces may hold promise for the miniaturization of optical systems containing polarization optics [11] resulting in new imaging polarimeter architectures for remote sensing and other applications. However, this is contingent on the success with which metasurface-based instrumentation can be calibrated and produce quantitatively accurate polarization data. This work highlights the practical considerations involved in doing so.

APPENDIX A: FLAT FIELDING THE SENSOR

CMOS sensors experience temperature-dependent fixed pattern noise in the form of dark signal non-uniformity and pixel response non-uniformity. Once a cooled CMOS sensor reaches thermal equilibrium, its non-uniform effects can be characterized by measuring each pixel's responsivity R and dark image I^{dark}. This work uses a procedure that is a modified version of the variable continuous illumination flat fielding method with constant exposure time described in Fig. 4(a) of EMVA Standard 1288 [15]. Instead of calibrating to an absolute radiant exposure per pixel, the calibration of pixel responsivity is referenced to a relative overall power as detected by a calibrated photodiode placed at a port in the integrating sphere. This method of relative power measurement is acceptable for polarimetric accuracy studies that assess the normalized Stokes parameters. Radiometric accuracy inclusive studies would require tracking absolute power.

Fluctuations in the LED illumination source output are tracked using this calibrated reference photodetector. The illumination across the entire sensor is assumed to be uniform, which follows from assuming the integrating sphere is ideal, and is represented by the power output by the LED source, p. This power is varied from zero to the highest level of output power before sensor saturation. In this work, the illumination power is varied from 5% to 95% of the saturation power in 5% steps to characterize the variation in pixel responsivity, $R_{m,n}$.

The relationship between power measured p, the pixelwise responsivity map R, and the input image I over an ROI on the sensor is

$$p = RI \tag{A1}$$

for each (m, n) pixel on an $M \times N$ pixel sensor. Equation (A1) represents a pixelwise multiplication. The image I is an average image over $L = 200$ individual frames and is formed by subtracting the dark image I^{dark} from the raw image I^{raw} and scaling by the source power's fluctuation, p^{Ref}, as measured by the photodiode at the integrating sphere:

$$I = \frac{1}{L}\sum_{l=0}^{L}\frac{p_0^{\mathrm{Ref}}}{p_l^{\mathrm{Ref}}}(I_l^{\mathrm{raw}} - I^{\mathrm{dark}}). \tag{A2}$$

The raw image is the average image over 100 frames as captured by the sensor without any corrections applied. The dark image is the average sensor response over 100 frames measured at a particular exposure when no light is incident. The full field is assumed to be uniformly illuminated by the integrating sphere, so p^{Ref} are applied as a uniform scale factor across the entire sensor to correct for fluctuations in the illumination source so they are not conflated with polarization effects. In this work, p_l^{Ref} is read from a list of power readings [μW] as detected by the external photodetector mounted at one of the integrating sphere's ports. The illumination source is driven at a nominally stable 100% output power. However, real-world fluctuations in illumination source stability are measurable, so $p_l^{\mathrm{Ref}} = p_l/p_0$ is used to track these fluctuations over L measurements to avoid conflating them with polarimetric effects.

The responsivity profile R for a given wavelength at a given exposure time is fit to Eq. (A1) as a simple line where the slope is proportional to responsivity. Sensor responsivity is calculated for each measurement waveband using 18 different illumination levels filling between 5% and 95% of the dynamic range of the sensor. Responsivity profiles are calculated for 460, 532, and 670 nm illumination for the exact exposure times used during the calibration, validation, and reference steps. These exposure times range from 6 to 800 ms. The effect of implementing this modified flat fielding procedure improved the validation versus reference DOLP agreement by up to 1%. The standard deviation of pixel values across a uniformly illuminated detector drops from approximately ±0.4% to approximately ±0.06% when the flat fielding procedure described above is applied.

APPENDIX B: PRACTICAL ALIGNMENT AND PROCESSING PROCEDURES

1. Avoiding Fringes in the Tilted Plate Test

The original tilted plate test procedure in [30] includes a collimation lens between incident illumination and the tilting glass plate. When used in conjunction with an imaging system and a quasi-monochromatic extended illumination source, a collimation lens produces fringes that obfuscate the low DOLP residuals assessed by this method. To prevent this issue, the plane-parallel plate target is directly illuminated by light from an LED that has passed through a 101.6 mm integrating sphere, in the same manner described in [23]. By directly imaging the integrating sphere, the number of components that could induce complex polarization artifacts is minimized.

To limit backreflection artifacts, adjustable irises were placed in the optical path, and all in-line rotating retarders and linear polarizers were selectively tilted between 1° and 3°.

2. Sub-Pixel Registration of Diffracted Orders

The final calibration technique in this work registers each diffraction order to a 1/4 pixel alignment accuracy using the one-time alignment method. A sub-pixel image registration was attempted in gradually finer resolution using *phase_cross_correlation()* [39] (from scikit-image version 1.7.1 [40]). The ideal sub-pixel accuracy alignment is 1/20 pixel [45], but no alignment accuracy finer than 1/4 pixel could be achieved. This alignment limit likely arises from the four diffracted orders, each striking a different quadrant of the imaging optics. Each order experiences slightly different lens aberrations that change the shape of the orders from a circle to a subtle oval.

The output of the registration gives the center in the image of each order in fractional pixels. The full detector image is shifted by a non-integer number of pixels using spline interpolation as implemented by SciPy's *ndimage.shift*(). Subsequently, each order in the shifted image is cropped to size, enabling the calculation of a Stokes image.

3. Auto-Correlation to Correct Beam Wander

Wedge in any rotating components will cause the beam to wander over the FOV of a sensor. Auto-correlation-based alignment can address this problem, but only when applied in a way that does not create artifacts. The 50 image linear Stokes metagrating calibration, 50 image linear Stokes reference, 50 image full Stokes metagrating calibration, and 16 image full Stokes reference measurement sets all contain rotating elements with a large enough wedge to induce beam wander. It is then tempting to perform image registration frame by frame to correct for this undesired effect. This section briefly discusses the differences in applying a frame-by-frame versus one-time alignment procedure.

The first step of both alignment methods co-registers the diffracted first orders onto one another using auto-correlation (as described in the previous section). In "one-time alignment," a calibration matrix $\mathbf{W}$ is calculated for each pixel in the resulting Stokes image using the same set of four pixels from the detector in all calibration frames. "Frame-by-frame alignment" adds an extra step that treats the zeroth image of the measurement set as the positional reference image. Each subsequent frame in the measurement set is aligned to this reference image. Then, the pixel located in the same relative position on the zeroth frame is extracted in all subsequent frames to calculate $\mathbf{W}$. This results in measurements from different neighboring pixels on the detector being used as the continuous output of one pixel during calibration. Figure 12 illustrates these two methods of alignment.

At first glance, frame-by-frame alignment may appear as the superior method for addressing beam wander. However, the final operation of a metagrating camera is a snapshot procedure. Any beam wander in one diffracted order is also observed in the other diffracted orders, so the relative clarity of the images is preserved as long as the combined metagrating and pixel responsivity of each point on the detector is well calibrated. This means that each individual pixel in each order should be treated independently of its neighbors in all downstream analyses. Attempting to correct beam wander using

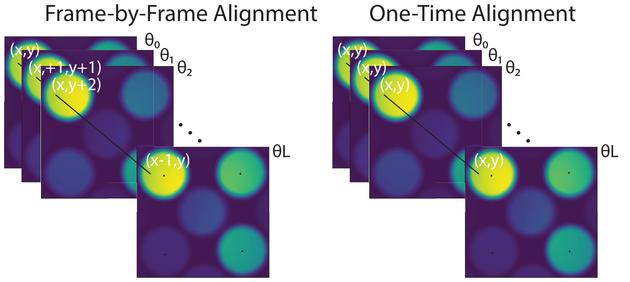

Fig. 12. Line through each measurement set indicates how a series of L images is compiled for one particular pixel. Frame-by-frame alignment treats the θ_0 frame as the reference image. Each subsequent lth frame is aligned to the reference using phase cross correlation. This approach produces a clearer calibration matrix image, but at the cost of generating the polarization artifacts that appear as a wrinkle pattern in Fig. 13. The resulting calibrated instrument matrix $\mathbf{W}$ does not match the snapshot operation of our division-of-amplitude metagrating camera concept. One-time alignment produces a $\mathbf{W}$, which stops alignment after the shared first step of determining the center of each order and referencing them to one another. Systems without beam wander on the detector do not face this alignment problem.

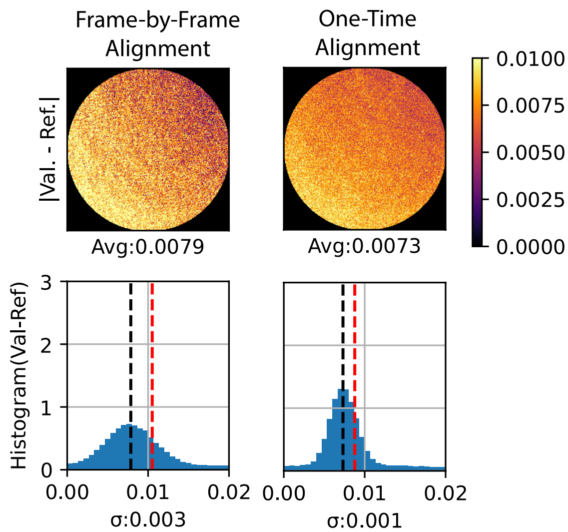

Fig. 13. $|\Delta\text{DOLP}| = |\text{Val. DOLP} - \text{Ref. DOLP}|$ images and corresponding histograms of errors are given for two cases: (left) when sub-pixel registration is applied on a frame-by-frame basis across all 50 calibration images in a sequence and (right) when sub-pixel registration is applied only to register the positions of the diffraction orders relative to one another. Proper application of a one-time alignment procedure during calibration improves the standard deviation of $|\Delta\text{DOLP}|$. When a frame-by-frame alignment is applied, the resulting ΔDOLP image also exaggerates the size of small artifacts in the field of view under observation.

frame-by-frame alignment produces polarization artifacts by treating the response of multiple neighboring pixels as sharing the responsivity of one pixel, which is ultimately problematic. Over L measurements, this appears as a fixed pattern noise polarization artifact. Figure 13 is an example of these artifacts as seen in ΔDOLP and ΔDOP images when observing an ostensibly uniform target (integrating sphere output port through a tilted glass plate). These artifacts arise from the remaining subtle pattern even after the flat fielding procedure described in Appendix A is applied. Flat fielding ideally corrects the subtle variation between pixels, but the real-world result is imperfect and only reduces the magnitude of these variations rather than eradicating them. The frame-by-frame method exacerbates the remaining noise into a wrinkle pattern that becomes a dominant feature as both a visible texture and an artificial numerical error in the ΔDOLP images.

APPENDIX C: FULL STOKES REFERENCE MEASUREMENT OPTIMIZATION

In this work, a custom $\lambda/3$ retarder for 532 nm is chosen to probe the analyzed full Stokes state of each diffraction order. A retardance magnitude between 127° and 132° is ideal for a sampling over the Poincaré sphere in a rotating retarder framework [41,42].

This work uses a $\delta = \lambda/3$ retarder under 532 nm illumination that is rotated in tandem with a linear polarizer with a relative rotation ratio r. We seek to optimize r so that the pair of retarder and polarizer can be used as a full Stokes, division-of-time reference polarimeter. To optimize r, we assess the condition number of the division-of-time combination for rotation ratios from zero to four, obtained using Eq. (C1). Angle θ_{offset} is the relative offset between the linear polarizer's transmission axis and the retarder's fast axis when both rotation motors are in the home position. This relative offset angle has a large influence on the condition number of the resulting $4 \times N$ polarimetric measurement matrix, $\mathbf{W}(r, \delta, \theta_{\text{offset}})$, which is defined by

$$\vec{W}_n(r, \delta, \theta_{\text{offset}}) = (\mathbf{LP}(r\theta_n + \theta_{\text{offset}})\mathbf{LR}(\delta, \theta_n))_{[0,:]}, \quad \text{(C1)}$$

where $\vec{W}_n$, the nth row of the polarimetric measurement matrix, is defined as the first row (analyzer vector) of the Mueller matrix formed by a linear retarder $\mathbf{LR}$ followed by a linear polarizer $\mathbf{LP}$. The Mueller rotation matrix

$$\mathbf{R}(\theta) = \begin{pmatrix} 1 & 0 & 0 & 0 \\ 0 & \cos(2\theta) & -\sin(2\theta) & 0 \\ 0 & \sin(2\theta) & \cos(2\theta) & 0 \\ 0 & 0 & 0 & 1 \end{pmatrix} \quad \text{(C2)}$$

is used to rotate any optical component about the z axis by θ. A linear retarder is

$$\mathbf{LR}(\delta, \theta) = \mathbf{R}(\theta) \begin{pmatrix} 1 & 0 & 0 & 0 \\ 0 & 1 & 0 & 0 \\ 0 & 0 & \cos(\delta) & \sin(\delta) \\ 0 & 0 & -\sin(\delta) & \cos(\delta) \end{pmatrix} \mathbf{R}(-\theta), \quad \text{(C3)}$$

where θ is the orientation of the fast axis, and δ is the retardance magnitude. A linear polarizer is

$$\mathbf{LP}(\theta) = \mathbf{R}(\theta)\frac{1}{2} \begin{pmatrix} 1 & 1 & 0 & 0 \\ 1 & 1 & 0 & 0 \\ 0 & 0 & 0 & 0 \\ 0 & 0 & 0 & 0 \end{pmatrix} \mathbf{R}(-\theta), \quad \text{(C4)}$$

where θ is the orientation of the transmission axis.

A well-chosen rotation ratio r will produce a $\mathbf{W}$ with a low condition number, which corresponds to lower SNR. Figure 14 plots the squared condition number $\text{cond}^2(\mathbf{W}(r, \delta, \theta_{\text{offset}}))$

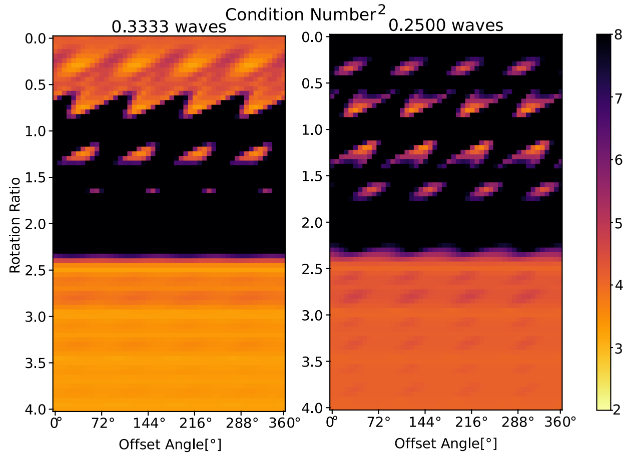

Fig. 14. Ideal rotation ratio r for a low SNR rotating retarder full Stokes analyzer should be unaffected by the θ_{offset} angle between the linear polarizer's transmission axis and the retarder's fast axis orientations when both rotation motors are in the home position. The polarimetric measurement matrix for a rotating retarder full Stokes analyzer is described by $\mathbf{W}(r, \delta, \theta_{\text{offset}})$ [Eq. (C1)]. The condition numbers squared of two instrument matrices are plotted above for a $\delta = \lambda/3$ retarder (left) and a $\delta = \lambda/4$ retarder (right). Condition numbers were calculated over rotation ratios between $r = 0.00$ and 4.00 as $\Delta r = 0.05$ and $\theta_{\text{offset}} = 0$ to 360°. Across both plots, the rotation ratio of $r = 2.5$ produced the minimum condition number over all θ_{offset} values.

over a series of rotation ratios for $\delta = \lambda/3$ and $\delta = \lambda/4$. The rotation ratio of $r = 2.5$ produced the smallest and most stable condition number over all θ_{offset} values for both $\delta = \lambda/3$ and $\delta = \lambda/4$ retarders.

APPENDIX D: ARTIFACTS, EDGE EFFECTS, AND ROI SELECTION

The limitation in the ROI used from the full FOV of the camera is due to edge effect artifacts that originate from the mechanical components required to construct the tilted glass plate experiment. Figure 15 depicts the artifacts that limited the accuracy test implementations. The images both span a 400 × 400 pixel ROI with the region within the image plotted in color indicating the 1″ outport of the integrating sphere. The outport spans a 400 pixel width in the 460 nm DOLP image, but this same outport spans a diameter equivalent to 440 pixels in the 532 nm DOP image.

In the linear Stokes calibration, a crosshatched pattern resembling fringes is present across all orders in all wavelengths. The crosshatch features correspond to a defocused image of the 250 × 250 nm write fields of the metagrating as written by the electron beam lithography tool. This pattern would not be present in the final image if the metagrating was placed exactly in the stop of the camera objective—a position not accessible in the off-the-shelf objective used in this work. This subtle fringe-like pattern is also visible near the top of the full Stokes calibration DOP image.

At the edges of the color image are concentric rings that limit the FOV of the image. These are the threads of the lens tube and the rotation motor that appear as a defocused image just beyond

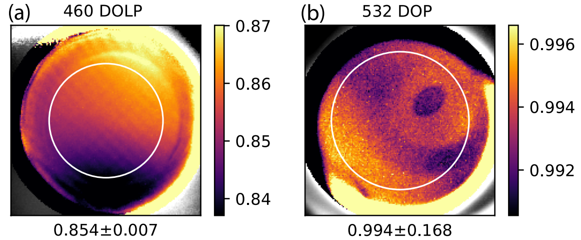

Fig. 15. Detailed examples of artifacts visible in just one diffraction order in (a) linear Stokes and (b) full Stokes calibrations of 460 and 532 nm metagratings, respectively. The white circles within each image indicate the ROIs that the linear and full Stokes calibration accuracies are calculated over. The 460 DOLP image contains a cross-hatching artifact that corresponds to a defocused image of the metagrating's stitching pattern, which is a byproduct of subtle miscalibration of the electron beam lithography tool used to fabricate these metagratings. Outside the area denoted by the white circle are the illuminated and defocused threaded rings of the rotation motors that the polarization optics are mounted in. The 532 DOP image contains all previously mentioned defocused artifacts in addition to a dark spot and circular artifact within the white circle, which corresponds to backreflections between the traditional polarization optics that comprise the full Stokes test setup.

the edge of the rotation motor's clear aperture. The effect of light scattering from these defocused threads is unavoidable due to the stage's position in the setup.

The spots in the 532 nm calibration's DOP correspond to dust and defects that cannot be removed from the linear polarizers used in this work without damaging their performance.

APPENDIX E: ABSOLUTE EFFICIENCY DATA

In the calibration study that occupies the bulk of this work, the grating's absolute efficiency is not explicitly considered; whatever the efficiency is, as long as it is constant, its effect can be accounted for (in camera units) during the calibration process. However, as a polarimetric technology, the efficiency of the grating is of interest for two reasons: first, as described in Appendix F, more photons will increase the shot-noise-limited fidelity of a measurement with a fixed integration time; second, a higher efficiency reduces stray light in the system, since light not directed into the inner four orders is directed into the transmitted and reflected zero diffraction orders, higher diffraction orders in the transmitted and reflected halfspaces, and reflected orders guided in the glass substrate.

Figure 16(b) shows simulated and measured efficiency data for the three gratings considered in this work (introduced in Fig. 2). Here, "efficiency" is taken to be the fraction of incident power directed to a given diffraction order when incoming light is unpolarized (i.e., the first element of the order's $\vec{D}_n$). The simulations and measurements shown in Fig. 16 pertain to collimated, normally incident light. This work studied the metagrating as a component in an imaging application, so the light interfacing with the metasurface is not always normally incident. For the full FOV of ±3°, the efficiency of the metagrating drops by only up to 0.9% for 460 nm, 7.3% for 532 nm, and 1.1% for 670 nm. A more detailed diagram of this efficiency figure is available in Section A of Supplement 1.

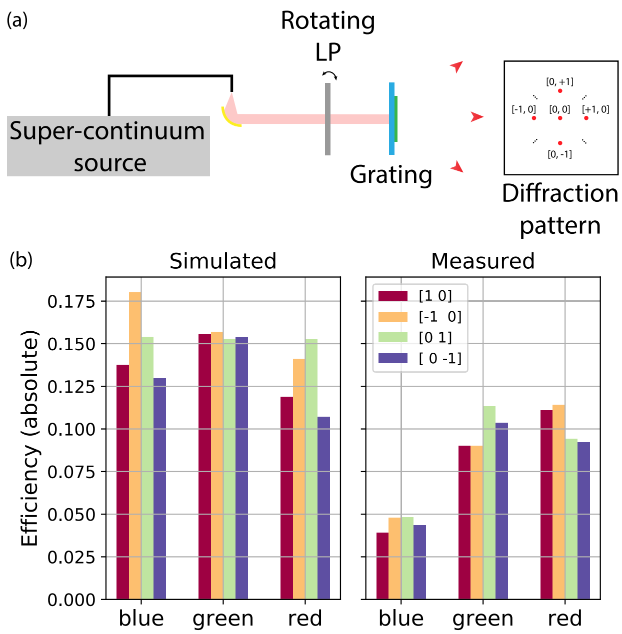

	blue	green	red
Simulated	0.601	0.619	0.520
Measured	0.179	0.398	0.411

Fig. 16. Metasurface grating efficiency measurement. (a) Light of variable wavelength from a fiber-coupled supercontinuum laser source is collimated and illuminates the metasurface grating through a rotatable linear polarizer. The fraction of incident light directed to the inner four orders is measured for a set of orthogonal linear polarization states and averaged to yield an efficiency (giving the fraction of light directed to an order for unpolarized light incidence). (b) For each of the three samples (blue, green, and red), the efficiency of each of the four orders is shown for the design as simulated using finite-difference time domain simulation (FDTD, left) and as-measured (right). A table gives the sum efficiency for all four orders for both cases. The simulation only reports efficiencies from the glass–air interface the metasurface lies upon; thus, an additional 4% loss from the first air–glass interface into the substrate should be subtracted from the simulated result when comparing it to the real life measurement.

The left barchart depicts the efficiency of each of the inner four orders from finite-difference time domain (FDTD) simulation of the ideal design. Two successive FDTD simulations are performed with x and y linearly polarized plane wave illumination; the efficiencies shown in Fig. 16(b) represent the average of the two, mimicking unpolarized light illumination.

The right barchart depicts the same measured experimentally on the fabricated gratings. This is carried out using the setup depicted in Fig. 16(a). Mirror-collimated light from a wavelength-tunable supercontinuum laser illuminates the grating (while being careful to *underfill* the grating aperture), and the fraction of incident light directed to each of the four orders is measured with a power meter. This is done for two orthogonal orientations of the linear polarizer, and the results shown in Fig. 16(b) represent the average of the two configurations, again mimicking unpolarized illumination.

A table at the bottom of Fig. 16(b) shows the sum efficiency of the four orders in simulation and measurement, representing the fraction of incident power actually used in the accuracy studies above. The deviation of these between simulation and measurement stems from the discrepancy between the designed and fabricated structures in Fig. 2; the simulated efficiencies, moreover, do not represent those maximally achievable if improved design strategies were to be employed.

APPENDIX F: SHOT NOISE AND ERROR BUDGETING

All of the studies reported in this work have been conducted in laboratory conditions with significant averaging of all data collected. Therefore, the accuracy results presented here primarily reflect the success with which a metasurface-based instrument can be calibrated, and the errors that remain are thus primarily *systematic* in nature. However, in any application, certain random errors will exist as well, chief among these being shot noise. Shot noise—a consequence of the discrete nature of light—will manifest as an uncertainty in any intensity measurement $\sigma_I = \sqrt{N}$, with N the number of collected photons, itself dictated by integration time and the photon flux hitting a detector. Shot noise governs the achievable accuracy of any polarimeter under a given measurement condition, even given perfect calibration.

Here, we show how the effect of shot noise can be predicted and budgeted in the design of a metasurface-based imaging polarimeter (though the analysis here is not specific to metasurface-based polarimeters *per se*). This is highly contextual, since the details of a given use case dictate the strength of illuminating light and what constitutes an acceptably long integration time. As an example here, we consider a metasurface-based polarimeter looking downwards at a sunlit cloud scene, an important practical application of polarimeters generally and a good example of how such an analysis can be undertaken for a specific situation.

The analysis proceeds in two discrete parts. First, the parameters of the problem are used to determine the number of photons illuminating a single pixel of the reconstructed polarization image in a back-of-the-envelope radiometric analysis. This alone dictates the random fluctuations in measured intensity due to shot noise. Second, these variations can be propagated through the polarimetric retrieval process and downstream to any derived polarimetric quantities.

1. Flux through Camera Entrance Pupil

The situation analyzed here is sketched in Fig. 17(a). The solar radiance $[\mathrm{W}/(\mathrm{m}^2 \cdot \mathrm{sr})]$ in the bandwidth measured by the camera is given by Planck's law as

$$L_{\mathrm{sun}} = \left(\frac{2hc^2}{\lambda^5 (e^{\frac{hc}{\lambda k_B T_{\mathrm{sun}}}} - 1)} \right) \Delta\lambda, \tag{F1}$$

where h is the Planck constant, c is the speed of light, k_B is the Boltzmann constant, and T_{sun} is the blackbody temperature of the Sun. The expression in parentheses gives the radiance per unit wavelength at center wavelength λ, which must be multiplied by the camera's spectral bandpass $\Delta\lambda$.

The solar irradiance $[\mathrm{W}/\mathrm{m}^2]$ (again, in this spectral bandpass) experienced at the "top of the atmosphere" (TOA) is given by

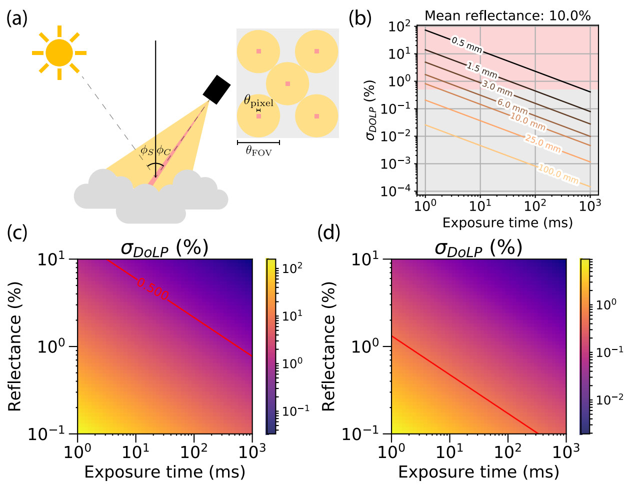

Fig. 17. Radiometric case study for cloud polarimetry and DOLP accuracy. (a) Defining the geometry of the problem. Sunlight illuminates a cloud scene at a zenith angle of ϕ_S viewed by a camera with a zenith angle of ϕ_C. (b) Expected DOLP uncertainty σ_{DOLP} for varying system entrance pupil diameters labeling each curve (in this case the size of the fabricated metasurface grating) for the parameters given in Table 3. (c) σ_{DOLP} for varying exposure times and object reflectances for a system with entrance pupil diameter $D_{\mathrm{EP}} = 3$ mm. A red line denotes the limit of $\sigma_{\mathrm{DOLP}} = 0.5\%$. (d) Same with $D_{\mathrm{EP}} = 20$mm.

$$E_{\mathrm{TOA}} = L_{\mathrm{sun}} \Omega_{\mathrm{SE}} \cos\phi_S, \tag{F2}$$

where Ω_{SE} is the solid angle subtended by the Sun viewed from the Earth, and ϕ_S is the solar zenith angle. Incident sunlight is assumed to interact with a layer of clouds, which in this simple analysis is taken to be Lambertian with a reflectance ρ. By definition, then, the radiance of the cloud layer [W/(m^2 · sr)] is then given by [46]

$$L_{\mathrm{cloud}} = \frac{\rho E_{\mathrm{TOA}}}{\pi}. \tag{F3}$$

The metasurface polarimeter will image the cloud scene over some full FOV θ_{FOV}. Incoming light from this FOV will distribute over several sub-images. However, the relevant FOV for this analysis is actually the FOV imaged by a single pixel of the output image. Here, we will compute the number of photons arriving from the region imaged by one pixel of the output polarization image, or equivalently, the number of photons incident on the four pixels whose measurements contribute to a single pixel of the reconstructed image.

Assuming the camera is focused at ∞, we can write (for a pixel at the center of the FOV) that

$$\theta_{\mathrm{pixel}} = 2\arctan\frac{p}{2f}, \tag{F4}$$

where p is the side dimension of a single pixel, and f is the camera lens' focal length. Then, the solid angle subtended by θ_{FOV}, i.e., the solid angle of a cloud scene collected by a single pixel, is given by

$$\Omega_{\mathrm{cloud,pixel}} = 4\pi \sin^2\frac{\theta_{\mathrm{pixel}}}{4}. \tag{F5}$$

The irradiance [W/m^2] experienced at the camera's EP for light collected by this single pixel is then given by

$$E_{\mathrm{camera}} = L_{\mathrm{cloud}} \Omega_{\mathrm{cloud,pixel}} \cos\phi_C, \tag{F6}$$

where ϕ_C is the viewing zenith angle of the camera.

Finally, the number of photons contributing to a single pixel of the output image is given by

$$P = \eta E_{\mathrm{camera}} \pi \left(\frac{D_{\mathrm{EP}}}{2}\right)^2 \Delta t \frac{\lambda}{hc}. \tag{F7}$$

Equation (F7) represents a product of the irradiance E_{camera}, an efficiency factor η representing the product of all transmission efficiencies in the system (the metasurface's η_M, that of the imaging optics η_O, and also the sensor's quantum efficiency η_S), the area of the EP with diameter D_{EP}, integration (exposure) time Δt, and a photon energy conversion factor.

Suppose light illuminating that pixel is assumed to have a Stokes vector $\mathbf{S}$ (whose first element S_0 would be the above photon number P); the photons directed to each of the four sub-pixels in the four imaging quadrants is given by

$$\vec{I} = \mathbf{AS}, \tag{F8}$$

with $\mathbf{A}$ the polarimetric measurement matrix and $\vec{I}$ a vector of photon fluxes at each of the four pixels corresponding to a single "pixel" of the final, reduced Stokes image.

2. Error Propagation

The uncertainty of each intensity measurement in $\vec{I}$ is given by the square root of its value in accordance with Poisson statistics. We can then write the covariance matrix of the measured intensity as

$$\mathrm{cov}(\vec{I}) = \mathrm{diag}\left(\sqrt{\vec{I}}\right). \tag{F9}$$

The 4×4 covariance matrix of $\vec{I}$ is a diagonal matrix with the square roots of $\vec{I}$'s entries on the diagonal.

Given that $\mathbf{S} = \mathbf{A}^{-1}\vec{I}$, if there is *no calibration error* (i.e., the elements of $\mathbf{A}$ have no uncertainty) then the uncertainty propagates through the linear system as

$$\mathrm{cov}(\mathbf{S}) = \mathbf{A}^{-1}\mathrm{cov}(\vec{I})(\mathbf{A}^{-1})^T, \tag{F10}$$

where $\mathrm{cov}(\mathbf{S})$ is the 4×4 covariance matrix of the determined Stokes vector at a pixel of the scene and is a generalized error metric of the determined polarization state, containing uncertainties of each component and their covariances.

If some scalar quantity $f(\mathbf{S})$ is then derived from $\mathbf{S}$, the variance of the quantity f due to random variations in $\mathbf{S}$ can be written as

$$\sigma_f = \sqrt{\vec{j}_f \mathrm{cov}(\mathbf{S}) \vec{j}_f^{\,T}}, \tag{F11}$$

where $\vec{j}_f(\mathbf{S})$ is the Jacobian vector for the quantity $f(\mathbf{S})$, with

$$\vec{j}_f(\mathbf{S}) = \vec{\nabla}_{\mathbf{S}} f = \left(\frac{\partial f}{\partial S_0}, \frac{\partial f}{\partial S_1}, \frac{\partial f}{\partial S_2}, \frac{\partial f}{\partial S_3}\right). \tag{F12}$$

For example, for the case of $\mathrm{DOLP}(\mathbf{S}) = \sqrt{S_1^2 + S_2^2}/S_0$,

Table 3. Parameters Used for Shot-Noise-Limited DOLP Accuracy Case Study Discussed in Appendix F and Fig. 17

Parameter	Description	Value
ρ	Cloud scene reflectance	0.1
λ	Center imaging wavelength	550 nm
$\Delta\lambda$	Bandpass of imaging bandwidth	5 nm
ϕ_S	Solar zenith angle	0°
ϕ_C	Camera zenith angle	0°
f	Lens focal length	16 mm
η_M	Metasurface efficiency factor	0.4
η_O	Optics efficiency factor	0.8
η_S	Sensor quantum efficiency	0.72
p	Pixel side length	3.45 µm

$$\vec{j}_{\mathrm{DOLP}}(\mathbf{S}) = \left(-\frac{\sqrt{S_1^2+S_2^2}}{S_0^2}, \frac{S_1}{S_0\sqrt{S_1^2+S_2^2}}, \frac{S_2}{S_0\sqrt{S_1^2+S_2^2}}, 0 \right). \tag{F13}$$

3. Numerical Example

Here, we apply the analysis above to the metasurface polarimeter of this work, as though it were being used as a downward-looking cloud polarimeter. For each of the parameters defined above, we use the values given in Table 3. We take a moderate effective reflectance of $\rho = 10\%$, and borrow the lens focal length, pixel side length, sensor quantum efficiency, and metasurface efficiency (the best case) from the camera studied in this work.

In Fig. 17(b), σ_{DOLP} is plotted as a function of exposure time Δt for the cloud scene with $\rho = 10\%$. The red region of the plot denotes $\sigma_{\mathrm{DOLP}} \geq 0.5\%$, while the gray region corresponds to $\sigma_{\mathrm{DOLP}} < 0.5\%$. Several curves correspond to varying instrument EP diameters; in the camera of this work, this diameter is simply the size of the metasurface grating (which is the EP), though depending on optics that may precede the metasurfaces in other implementations, this would not necessarily remain the case [13]. As expected, the larger the light-collecting EP, the more robust to random errors in measured DOLP the instrument will be at all exposure times. For this ρ, a ∼cm scale metasurface grating would have sufficient light collection to suppress random DOLP to the degree desired for atmospheric science applications over the entire range of exposure times considered; the 3 mm grating used in this work, on the other hand, is "safe" only above 20 ms.

In Figs. 17(c) and 17(d), σ_{DOLP} is computed now as a function not only of exposure time Δt, but also of the scene's reflectance ρ. In Fig. 17(c), $D_{\mathrm{EP}} = 3$ mm, while in (d), $D_{\mathrm{EP}} = 20$ mm. In both, a red contour line denotes where $\sigma_{\mathrm{DOLP}} = 0.5\%$; to the right and above this line (i.e., at longer exposure times and for brighter objects), $\sigma_{\mathrm{DOLP}} < 0.5\%$. For a 3 mm metasurface grating, only somewhat bright objects ($\rho \geq 1\%$) can be imaged unless long exposures (longer than hundreds of ms) are employed. A 2 cm collection aperture, on the other hand, presents the ability to obtain the DOLP at the desired accuracy for even dim objects ($\rho \sim 0.1\%$) in under 100 ms.

What constitutes an acceptable integration time is also context dependent, depending on the dynamics of a given application. For atmospheric polarimetry, where ideally km-scale resolution is desired from low Earth orbit (LEO), an exposure time should be low enough that motion artifacts from the orbit during Δt do not constitute more than a few individual pixels of spatial resolution. Since in LEO groundspeed is approximately 8 km/s, exposures would ideally be 125 ms or less.

We have performed the photon-counting analysis here at the single photon level. However, adjacent pixels can be spatially binned to decrease random errors due to shot noise (at the expense of spatial resolution). This is the approach taken in some atmospheric polarimeters (e.g., the upcoming MAIA instrument [23]) to meet the target accuracy of $\sigma_{\mathrm{DOLP}} \leq 0.5\%$.

In conclusion, random noise can enter into the polarimetric measurement process, adding errors to the measured polarization state above and beyond those from miscalibration. Any attempt to account for this is application specific, since these depend on illumination level and the details of the light-collecting ability of a given instrument. We have shown here how random errors can be budgeted for in a specific application, namely, atmospheric polarimetry. This type of analysis reveals the combination of design parameters necessary to reduce random errors to a sufficient degree that they become insignificant relative to errors due to miscalibration/data reduction, which themselves can be characterized experimentally using the methods of this work.

Funding. National Aeronautics and Space Administration (80NSSC20K0318, 80NSSC21K0799); National Science Foundation (ECCS-2025158).

Acknowledgment. We thank Dr. Paul Chevalier (Harvard University) for helpful comments. This work was performed in part at the Harvard University Center for Nanoscale Systems (CNS), a member of the National Nanotechnology Coordinated Infrastructure Network (NNCI), which is supported by the NSF.

Disclosures. NAR: Metalenz, Inc. (I, E, C, P, R), MJ: NIL Technology ApS (E), FC: Metalenz, Inc. (I, S).

Data availability. Data underlying the results presented in this paper are not publicly available at this time but may be obtained from the authors upon reasonable request.

Supplemental document. See Supplement 1 for supporting content.

REFERENCES

1. J. S. Tyo, D. L. Goldstein, D. B. Chenault, and J. A. Shaw, "Review of passive imaging polarimetry for remote sensing applications," Appl. Opt. **45**, 5453–5469 (2006).
2. F. Snik, J. Craven-Jones, M. Escuti, S. Fineschi, D. Harrington, A. De Martino, D. Mawet, J. Riedi, and J. S. Tyo, "An overview of polarimetric sensing techniques and technology with applications to different research fields," Proc. SPIE **9099**, 90990B (2014).
3. P. Y. Deschamps, J. C. Buriez, F. M. Bréon, M. Leroy, A. Podaire, A. Bricaud, and G. Sèze, "The POLDER mission: instrument characteristics and scientific objectives," IEEE Trans. Geosci. Remote Sens. **32**, 598–615 (1994).
4. O. Dubovik, Z. Li, M. I. Mishchenko, *et al.*, "Polarimetric remote sensing of atmospheric aerosols: Instruments, methodologies, results, and perspectives," J. Quant. Spectrosc. Radiat. Transfer **224**, 474–511 (2019).
5. J. O. Stenflo, "Instrumentation for solar polarimetry," in *Solar Magnetic Fields: Polarized Radiation Diagnostics* (Springer Netherlands, 1994), pp. 312–350.

6. J. E. Wolfe and R. A. Chipman, "Polarimetric characterization of liquid-crystal-on-silicon panels," Appl. Opt. **45**, 1688–1703 (2006).
7. A. Kadambi, V. Taamazyan, B. Shi, and R. Raskar, "Polarized 3D: high-quality depth sensing with polarization cues," in *Proceedings IEEE International Conference on Computer Vision* (2015), pp. 3370–3378.
8. M. A. Sarwar, B. Bilbrey, and Z. Peng, "Polarized images for security," U.S. patent 9536362 B2 (3 January 2012).
9. N. Yu and F. Capasso, "Flat optics with designer metasurfaces," Nat. Mater. **13**, 139–150 (2014).
10. A. H. Dorrah and F. Capasso, "Tunable structured light with flat optics," Science **376**, eabi6860 (2022).
11. N. A. Rubin, Z. Shi, and F. Capasso, "Polarization in diffractive optics and metasurfaces," Adv. Opt. Photon. **13**, 836–970 (2021).
12. N. A. Rubin, G. D'Aversa, P. Chevalier, Z. Shi, W. T. Chen, and F. Capasso, "Matrix Fourier optics enables a compact full-Stokes polarization camera," Science **365**, eaax1839 (2019).
13. N. A. Rubin, P. Chevalier, M. Juhl, M. Tamagnone, R. Chipman, and F. Capasso, "Imaging polarimetry through metasurface polarization gratings," Opt. Express **30**, 9389–9412 (2022).
14. P. A. Williams, S. M. Etzel, J. D. Kofler, and C.-M. Wang, "Standard reference material 2538 for polarization-mode dispersion (non-mode-coupled)," in *NIST Special Publication* (2002), pp. 145–260.
15. European Machine Vision Association, "EMVA standard 1288 standard for characterization of image sensors and cameras," Tech. Rep. (European Machine Vision Association, 2021).
16. I. S. Organization, "Optics and optical instruments—microscopes—reference system of polarized light microscopy," Tech. Rep. ISO 8576:1996 (International Standards Organization, 1996).
17. J. L. Deuzé, F. M. Bréon, C. Devaux, P. Goloub, M. Herman, B. Lafrance, F. Maignan, A. Marchand, F. Nadal, G. Perry, and D. Tanré, "Remote sensing of aerosols over land surfaces from POLDER-ADEOS-1 polarized measurements," J. Geophys. Res. **106**, 4913–4926 (2001).
18. D. Tanré, F. M. Bréon, J. L. Deuzé, O. Dubovik, F. Ducos, P. François, P. Goloub, M. Herman, A. Lifermann, and F. Waquet, "Remote sensing of aerosols by using polarized, directional and spectral measurements within the A-Train: the PARASOL mission," Atmos. Meas. Tech. **4**, 1383–1395 (2011).
19. J. V. Martins, R. Fernandez-Borda, B. McBride, L. Remer, and H. M. J. Barbosa, "The Harp hyperangular imaging polarimeter and the need for small satellite payloads with high science payoff for earth science remote sensing," in *IEEE International Geoscience and Remote Sensing Symposium (IGARSS)* (2018), pp. 6304–6307.
20. A. Puthukkudy, J. V. Martins, L. A. Remer, X. Xu, O. Dubovik, P. Litvinov, B. McBride, S. Burton, and H. M. J. Barbosa, "Retrieval of aerosol properties from Airborne Hyper-Angular Rainbow Polarimeter (AirHARP) observations during ACEPOL 2017," Atmos. Meas. Tech. **13**, 5207–5236 (2020).
21. B. A. McBride, J. V. Martins, H. M. J. Barbosa, W. Birmingham, and L. A. Remer, "Spatial distribution of cloud droplet size properties from Airborne Hyper-Angular Rainbow Polarimeter (AirHARP) measurements," Atmos. Meas. Tech. **13**, 1777–1796 (2020).
22. Y. Liu and D. J. Diner, "Multi-angle imager for aerosols: a satellite investigation to benefit public health," Public Health Rep. **132**, 14–17 (2017).
23. G. van Harten, D. J. Diner, B. J. Daugherty, B. E. Rheingans, M. A. Bull, F. C. Seidel, R. A. Chipman, B. Cairns, A. P. Wasilewski, and K. Knobelspiesse, "Calibration and validation of Airborne Multiangle SpectroPolarimetric Imager (AirMSPI) polarization measurements," Appl. Opt. **57**, 4499–4513 (2018).
24. D. J. Diner, S. W. Boland, M. Brauer, *et al.*, "Advances in multiangle satellite remote sensing of speciated airborne particulate matter and association with adverse health effects: from MISR to MAIA," J. Appl. Remote Sens. **12**, 042603 (2018).
25. B. Fougnie, T. Marbach, A. Lacan, R. Lang, P. Schlüssel, G. Poli, R. Munro, and A. B. Couto, "The multi-viewing multi-channel multi-polarisation imager–overview of the 3MI polarimetric mission for aerosol and cloud characterization," J. Quant. Spectrosc. Radiat. Transfer **219**, 23–32 (2018).
26. O. P. Hasekamp, G. Fu, S. P. Rusli, L. Wu, A. D. Noia, J. D. Brugh, J. Landgraf, J. M. Smit, J. Rietjens, and A. van Amerongen, "Aerosol measurements by SPEXone on the NASA PACE mission: expected retrieval capabilities," J. Quant. Spectrosc. Radiat. Transfer **227**, 170–184 (2019).
27. J. M. Smit, J. H. H. Rietjens, G. van Harten, A. Di Noia, W. Laauwen, B. E. Rheingans, D. J. Diner, B. Cairns, A. Wasilewski, K. D. Knobelspiesse, R. Ferrare, and O. P. Hasekamp, "SPEX airborne spectropolarimeter calibration and performance," Appl. Opt. **58**, 5695–5719 (2019).
28. O. P. Hasekamp and J. Landgraf, "Retrieval of aerosol properties over land surfaces: capabilities of multiple-viewing-angle intensity and polarization measurements," Appl. Opt. **46**, 3332–3344 (2007).
29. K. Knobelspiesse, B. Cairns, M. Mishchenko, J. Chowdhary, K. Tsigaridis, B. van Diedenhoven, W. Martin, M. Ottaviani, and M. Alexandrov, "Analysis of fine-mode aerosol retrieval capabilities by different passive remote sensing instrument designs," Opt. Express **20**, 21457–21484 (2012).
30. A.-B. Mahler and R. A. Chipman, "Polarization state generator: a polarimeter calibration standard," Appl. Opt. **50**, 1726–1734 (2011).
31. J. C. Kemp, R. D. Wolstencroft, and J. B. Swedlund, "Circular polarization: Jupiter and other planets," Nature **232**, 165–168 (1971).
32. K. Ichimoto, B. Lites, D. Elmore, *et al.*, "Polarization calibration of the solar optical telescope onboard HINODE," Sol. Phys. **249**, 233–261 (2008).
33. R. A. Chipman, W.-S. T. Lam, and G. Young, *Polarized Light and Optical Systems* (CRC Press, 2019).
34. A. Arbabi, Y. Horie, M. Bagheri, and A. Faraon, "Dielectric metasurfaces for complete control of phase and polarization with subwavelength spatial resolution and high transmission," Nat. Nanotechnol. **10**, 937–943 (2015).
35. J. P. B. Mueller, N. A. Rubin, R. C. Devlin, B. Groever, and F. Capasso, "Metasurface polarization optics: independent phase control of arbitrary orthogonal states of polarization," Phys. Rev. Lett. **118**, 113901 (2017).
36. N. A. Rubin, A. Zaidi, A. H. Dorrah, Z. Shi, and F. Capasso, "Jones matrix holography with metasurfaces," Sci. Adv. **7**, eabg7488 (2021).
37. A. Zaidi, N. A. Rubin, A. H. Dorrah, J.-S. Park, and F. Capasso, "Generalized polarization transformations with metasurfaces," Opt. Express **29**, 39065–39078 (2021).
38. R. C. Devlin, M. Khorasaninejad, W.-T. Chen, J. Oh, and F. Capasso, "Broadband high-efficiency dielectric metasurfaces for the visible spectrum," Proc. Natl. Acad. Sci. USA **113**, 10473–10478 (2016).
39. M. Guizar-Sicairos, S. T. Thurman, and J. R. Fienup, "Efficient subpixel image registration algorithms," Opt. Lett. **33**, 156–158 (2008).
40. S. van der Walt, J. L. Schönberger, J. Nunez-Iglesias, F. Boulogne, J. D. Warner, N. Yager, E. Gouillart, T. Yu, and the scikit-image contributors, "Scikit-image: image processing in Python," PeerJ **2**, e453 (2014).
41. M. H. Smith, "Optimization of a dual-rotating-retarder Mueller matrix polarimeter," Appl. Opt. **41**, 2488–2493 (2002).
42. D. S. Sabatke, M. R. Descour, E. L. Dereniak, W. C. Sweatt, S. A. Kemme, and G. S. Phipps, "Optimization of retardance for a complete Stokes polarimeter," Opt. Lett. **25**, 802–804 (2000).
43. T. A. Germer, "Full four-dimensional and reciprocal Mueller matrix bidirectional reflectance distribution function of sintered polytetrafluoroethylene," Appl. Opt. **56**, 9333–9340 (2017).
44. R. Azzam, I. Elminyawi, and A. El-Saba, "General analysis and optimization of the four-detector photopolarimeter," J. Opt. Soc. Am A **5**, 681–688 (1988).
45. M. H. Smith, J. B. Woodruff, and J. D. Howe, "Beam wander considerations in imaging polarimetry," Proc. SPIE **3754**, 50–54 (1999).
46. J. M. Palmer and B. G. Grant, *The Art of Radiometry* (SPIE, 2010).